Energy & Environmental Science

ROYAL SOCIETY OF CHEMISTRY

PAPER

View Article Online
View Journal | View Issue

Cite this: *Energy Environ. Sci.*, 2026, **19**, 3283

Conformal hetero-electrolyte interface between soft oxyhalides and garnet enables low-pressure lithium-reservoir-free solid-state batteries

Max Palmer, †[c] Vipin K. Singh, †[a] Leonardo Merola,[b] Karthikeyen Natarajan Pugazhendhi,[a] Pallab Barai,[d] Insang You,[a] Yubo Wang,[a] Eric Carlson,[c] Cathy Wang,[c] Hao Zheng,[c] Venkat Srinivasan,[d] Jürgen Janek,[b] Jeff Sakamoto*[c] and Linda F. Nazar*[a]

The operation of solid-state batteries with a lithium metal anode and a high voltage cathode requires solid electrolytes (SEs) that are chemically stable with lithium, have a wide electrochemical window, and accommodate volume changes in the electrodes. Unfortunately, no SE has exhibited satisfactory mechanical and electrochemical properties that fit these requirements to date. Dual solid electrolyte systems that use a different SE for the anolyte and catholyte present a viable solution. Here, we focus on oxyhalide SEs that demonstrate superior ionic conductivity and cathode compatibility, where their lithium metal reactivity and poor reduction stability can be resolved using a lithium garnet ($Li_{6.5}La_3Zr_{1.5}Ta_{0.5}O_{12}$, LLZTO) separator. Nonetheless, this imposes a new hetero-electrolyte (H-E) interface at the anolyte|catholyte contact that defines the ion transport across the boundary. We report its promising properties, which are deconvoluted from the electrical measurements of bilayer symmetric cells, for three representative oxyhalide catholytes, $LiNbOCl_4$, $LiTaOCl_4$, and $Li_3Al_3O_2Cl_8$. Pressure-dependent measurements reveal that the relative softness of the oxyhalides (hardness $\leq$0.4 GPa) enables H-E resistances lower than 150 Ω cm^2 at 2–3 MPa. Mesoscale modelling reveals that the transfer-active contact area of oxyhalides with LLZTO is about 2–3-fold higher than that of argyrodite, Li_6PS_5Cl. The low H-E resistance of the $LiNbOCl_4$|$Li_{6.5}La_3Zr_{1.5}Ta_{0.5}O_{12}$ dual electrolyte enables the cycling of a Li|$LiNi_{0.82}Mn_{0.07}Co_{0.11}O_2$ full cell with a high discharge capacity (200 mA h g^{-1}) at 60 °C and ~7 MPa. Importantly, we demonstrate a Li-reservoir-free full cell with high Coulombic efficiency (>99.5%) and capacity at 1 MPa using this approach coupled with a garnet-silver interlayer.

Received 24th December 2025,
Accepted 9th April 2026

DOI: 10.1039/d5ee07777j

rsc.li/ees

Broader context

Solid-state batteries can offer high energy densities and improved safety, but no solid electrolyte is simultaneously compatible with both a lithium metal anode and a high voltage uncoated cathode yet. Dual solid electrolyte (DSE) batteries are attractive because they can meet both requirements. However, the contact of different solid electrolyte layers introduces significant challenges associated with the resulting hetero-electrolyte (H-E) interface and can yield large resistances (>500 Ω cm^2) at low stack pressures, significantly hindering battery performance. Here, we report that H-E interface resistances down to 150 Ω cm^2 can be achieved at relatively low stack pressures (*i.e.*, 2–3 MPa) and 25 °C, with a combination of soft oxyhalide catholytes and garnet separator as anolytes. Mechanical analysis and mesoscale modelling reveal that oxyhalides (hardness ≤0.4 GPa) are significantly softer than sulfide and halide electrolytes, resulting in a larger transfer-active contact area at the oxyhalide|garnet H-E interface compared with a sulfide|garnet interface. Moreover, the H-E interfacial activation energy (E_a) closely matches the grain-boundary E_a of the garnet once the geometric current constriction is removed. We demonstrate that the DSE design with $LiNbOCl_4$ and $Li_{6.5}La_3Zr_{1.5}Ta_{0.5}O_{12}$ solid electrolytes allows for the incorporation of a high voltage cathode and a Li-reservoir-free anode. The DSE batteries achieve a high Coulombic efficiency (>99.7%) at 5 MPa and 60 °C over 120 cycles. This work demonstrates the potential for Li-reservoir-free DSE batteries at low pressures.

[a] *Department of Chemistry and the Waterloo Institute for Nanotechnology, University of Waterloo, N2L 3G1 Waterloo, Ontario, Canada. E-mail: lfnazar@uwaterloo.ca*
[b] *Institute of Physical Chemistry and Center for Materials Research (ZfM), Justus-Liebig-University, Giessen, Heinrich-Buff-Ring 17, D-35392 Giessen, Germany*
[c] *Materials Department & Department of Mechanical Engineering, 1355 University of California, Santa Barbara, CA 93106-5050, USA. E-mail: sakamoto@ucsb.edu*
[d] *Argonne National Laboratory, Lemont, IL, 60439, USA*
† These authors contributed equally.

Introduction

Solid-state batteries (SSBs) have gained significant research attention due to the growing demand for energy storage systems with high energy and power densities.[1] Lithium metal and ''anode-free,'' or more properly termed reservoir-free designs, have been extensively studied because they offer the possibility to simplify construction, cycle ultra-pure lithium, and enable the high cell energy density required for SSBs.[2–4] Significant efforts have focused on suppressing chemo-mechanical degradation at the anode|solid electrolyte (SE) interface, including dendrite growth, side reactions, and void formation.[3,5,6] On the cathode side of SSBs, nickel-rich $LiNi_xMn_yCo_zO_2$ ($x + y + z = 1$, NMC) offers high capacity and cell voltage, but a trade-off remains between chemical stability and mechanical compatibility at the cathode|SE interface due to highly oxidative environments and contact loss from the cathode particle volume change.[7–9] Different solid electrolytes have been explored for SSBs, where the most promising inorganic SE candidates can be categorized as oxyhalides/halides, oxides, and sulfides. Each has distinct chemical, electrochemical, and mechanical properties, yet no single SE meets all requirements to enable Li metal SSBs.[10,11]

The oxide $Li_{6.5}La_3Zr_{1.5}Ta_{0.5}O_{12}$ (LLZTO) allows the use of a lithium metal anode (LMA).[12–14] LLZTO is a brittle ceramic material with a high hardness and Young's modulus; due to the ductility of Li, it is possible to create and maintain intimate contact between the two, depending on the applied current density, temperature, and stack pressure.[15–21] However, there is limited compatibility of LLZTO with the existing oxide cathode materials.[7] Degradation reactions between the LLZTO and cathode materials arise during high-temperature processes, such as co-sintering, that are necessary to achieve good contact, which negatively impact performance.[22,23] Achieving and maintaining intimate interfacial contact in ''stiff'' oxide-based SSBs remains a major unresolved challenge. On the other hand, softer sulfide and halide electrolytes can achieve intimate contact with cathode materials under high fabrication pressure and moderate or room temperature, circumventing deleterious reactions. Although they are softer than oxides, they still require high external pressure to sustain interfacial contact during operation. Generally, the largest impediment to implementing sulfides and halides in SSBs is their chemical reactivity with a LMA.[24–27] Typically, alternative alloy anodes, such as Li–In, are employed to avoid reactions with Li, but this reduces the working voltage of the cell and the energy density.[28,29] Hardly any solid electrolyte is equally suited for reducing and oxidizing conditions at the LMA and cathode sides, respectively.

Recent investigations into cell concepts utilizing dual inorganic solid electrolytes aim to combine the benefits of different SEs.[29–32] There are numerous reports on sulfides as the anolyte and halides as the catholyte; however, there are few definitive studies that explore the interface between two inorganic SEs.[33–35] For a comprehensive review of different dual solid electrolytes explored, we refer the reader to the work by Lee *et al.*[36] Although LLZTO is a superior anolyte owing to its stability with Li, few studies have implemented it in dual electrolyte cells. In these cells, LLZTO acts as an anolyte in contact with the LMA and protects the catholyte from reduction, while a softer SE is used as the catholyte and forms intimate contact with the cathode active material. Dual solid electrolyte systems can meet the individual requirements for each electrode, but they introduce a new hetero-electrolyte (H-E) interface that may exhibit high resistances or activation energy barriers, thereby affecting charge transport. Factors affecting transport across such interfaces include the contact mechanics and surface topography.[34] These surface effects cause geometric current constriction as shown first by Fleig and Maier and then discussed for H-E interfaces by Eckhardt and Kremer *et al.*, who considered different ionic conductivities of the SEs, which govern the charge transport at the H-E interface.[37,38] Current constriction is significant at low stack pressures in LLZTO dual electrolyte cells and can be a major contribution to the total resistance.[33–35,39]

To be competitive with Li-ion batteries, achieving an H-E resistance below 20–40 Ω cm^2 remains crucial for the practical viability of dual electrolyte SSBs.[40–42] It remains difficult to achieve an H-E resistance near these values at relatively low stack pressures ($<$3–4 MPa) compared to the higher pressures used for halides and sulfides. Although a comprehensive guide on the practical pressures for SSBs has not been elucidated, a previous study by Janek and Zeier mentioned that a few MPa may be technically feasible, although 0.1 MPa is ideal to be comparable to conventional Li-ion batteries.[10] Soft solid electrolytes, such as the recently explored Li metal oxyhalides that include $LiNbOCl_4$ (LNOC), $LiTaOCl_4$ (LTOC), $Li_3Al_3O_2Cl_8$ (LAOC), as well as pliable $xLiCl\text{-}GaF_3$ composites, offer several advantages towards the realization of lower and practical stack pressures.[29,43–46] These advantages include a lower hardness, which facilitates densification and the ability to maintain conformal interfaces to improve cycling. Both of these aspects are simultaneously achieved potentially at moderate pressures ($\sim$7 MPa).[44,45] LNOC and LTOC also exhibit high ionic conductivity ($\sim$10 mS cm^{-1}), which enables thicker cathodes.

Herein, we report an in-depth study of the H-E interfaces of oxyhalide-based Li catholytes in contact with LLZTO in several cell configurations, in combination with numerous experimental techniques and computational analyses. Our study combines the mechanical property analysis of solid electrolytes *via* work of compression analysis and microindentation hardness measurements, interfacial analysis *via* X-ray photoelectron spectroscopy (XPS), and electrochemical analysis *via* electrochemical impedance spectroscopy (EIS) in symmetric and full cells with Li foil. We also study Li reservoir-free cells by employing a seeded silver interlayer to improve *in situ* anode formation and Coulombic efficiency. Our findings highlight the importance of achieving conformal contact under low stack pressures ($\sim$3–4 MPa) and demonstrate that ion transfer across the H-E interface is governed by the mitigation of the surface passivation layer (Li_2CO_3/LiOH) on LLZTO. Pressure-dependent resistance measurements support the current-constriction

concept at the H-E interface.[37,38] Phase-field-based meso-scale simulations were employed to compare the densification of argyrodite and oxyhalides at different fabrication pressures using their experimental hardness values. This approach reveals that the transfer-active contact area of LMOCs with LLZTO (*i.e.*, the H-E contact fraction) is about 2–3-fold higher than that of argyrodite Li_6PS_5Cl. Most importantly, we achieve low resistance, down to 150 Ω cm^2, at lower stack pressures (*i.e.*, 3–4 MPa) with the oxyhalides interfaced with LLZTO. A full cell utilizing single crystal $LiNi_{0.82}Mn_{0.07}Co_{0.11}O_2$ and LMA with an LNOC catholyte and LLZTO anolyte exhibits stable cycling behavior, serving as proof-of-concept for the oxyhalide|garnet dual electrolyte approach. The full cell performance is adversely affected by the oxidation of LNOC at high voltages, which is exacerbated by carbon additives. A Li reservoir-free design enabled by a seeded silver interlayer demonstrates a high Coulombic efficiency of 99.5% at 1 MPa and 60 °C. To the best of our knowledge, this study is the first to demonstrate a Li-reservoir-free solid-state cell employing an LLZTO separator without any ionic liquid or polymer at the cathode interface.

Results and discussion

Properties and densification of solid electrolytes

LLZTO and oxyhalides were prepared in-house and characterized using X-ray diffraction (XRD; Fig. S1) analysis to confirm the lack of noticeable LiCl impurities in the oxyhalides and the phase purity of LLZTO. The ionic conductivity σ_{Li^+} was measured by EIS in conventional symmetric cells (SS|LMOCs|SS; M = Nb, Ta, and Al; SS = stainless steel), and the activation energy E_a was evaluated at temperatures ranging from −40 °C to +40 °C. The σ_{Li^+} and E_a values are similar to those previously reported for LTOC and LNOC (Fig. S2; σ_{Li^+} = 7.8 mS cm^{-1}, E_a = 0.24 eV, 9 mS cm^{-1}, and 0.29 eV), LAOC (Fig. S2; 0.93 mS cm^{-1}, 0.46 eV), and LLZTO (Fig. S2; 0.8 mS cm^{-1}, 0.45 eV); see Methods for details.[29,44] To evaluate the densification of the LMOCs, SE pellets were fabricated using Li_6PS_5Cl (LPSCl) as a reference. Over 300 MPa is typically used for LPSCl,[39,47,48] but here we used lower fabrication pressures that are more suitable for LMOCs for comparison (*i.e.*, 120 MPa). Fig. 1 presents the focused ion beam scanning electron microscopy (FIB-SEM) cross-sectional images of the LAOC, LNOC, and LPSCl SEs after densification at 120 MPa for 3 minutes. The LAOC SE exhibits a nearly fully dense microstructure (Fig. 1a) with no observable porosity. In contrast, LNOC (Fig. 1b) and LTOC (Fig. S3) have relatively dense microstructures, while LPSCl exhibits a noticeably more porous microstructure (Fig. 1c). The relative densities obtained for LNOC and LPSCl were 96% and 74% based on theoretical densities of 2.61 g cm^{-3} and 1.64 g cm^{-3}, respectively.[44,49] The pronounced difference in relative density between LNOC and LPSCl can be attributed, at least in part, to differences in particle size distribution and the associated compaction behavior. The particle size strongly influences the elastic strain recovery upon unloading, as larger particles tend to store more elastic energy during pressing and exhibit greater spring-back once the load is removed, resulting in higher residual porosity. In contrast, smaller particles provide a higher contact area and undergo more effective plastic deformation at interparticle contacts, thereby retaining densification more efficiently after pressure release. Consequently, the comparatively lower relative density observed for LPSCl is consistent with the increased elastic recovery arising from its coarser particle characteristics.[50] Moreover, the theoretical densities of LAOC and LTOC could not be determined due to their

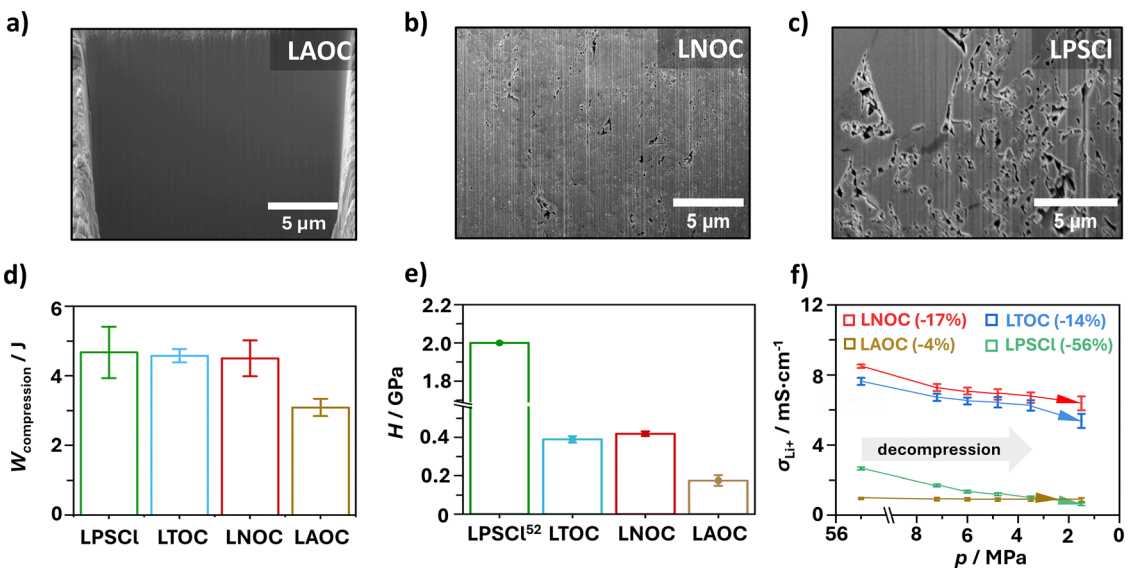

Fig. 1 FIB-SEM cross-sectional images of (a) LAOC, (b) LNOC and (c) LPSCl, after densification at 120 MPa for 3 minutes. (d) Densification behavior of SEs *vs.* work of compression performed up to a pressure of 310 MPa. (e) Hardness measurements of LPSCl (hot-pressed) using nano-indentation[52] and LMOC (M = Nb, Ta, and Al) SEs measured *via* microindentation. (f) Conductivity measurements during the unloading from 55 MPa to lower stack pressures for LTOC, LNOC, LAOC and LPSCl. The relative change (%) in the ionic conductivity upon releasing the stack pressure from 55 to 7.2 MPa is indicated in parentheses. Error bars represent the standard deviation from at least three measurements.

amorphous nature. The densification behavior of the electrolyte powder was further studied using an in-die compression test in a load frame (Instron) up to 300 MPa (Fig. S4).

The area under the force-displacement curve represents the work of compression needed to densify the powders (Fig. 1d).[51] LAOC has the lowest value of 3.1 J, compared to 4.5, 4.6, and 4.7 J for LTOC, LNOC, and LPSCl, respectively. The microindentation hardness values measured for LAOC, LNOC, and LTOC are 0.18, 0.42, and 0.38 GPa, respectively (Fig. 1e); the indentation maps and modulus measurements are illustrated in Fig. S5 and Table S1. The lower hardness of LAOC may be expected due to its viscoplasticity, while there are no reports on LNOC and LTOC demonstrating viscoplasticity.[43] Due to the porosity of our LPSCl, Fig. 1e compares the measured LMOC microindentation hardness with the literature value of LPSCl from nanoindentation.

Although related, it should be noted that hardness is typically strain rate-independent, while viscoplasticity is strain rate-dependent. In the future, the viscoplastic properties of LMOCs will be studied, specifically with regard to their impact on densification and cell cycling behavior. The reported hardness values for sulfide-type SEs measured *via* nanoindentation range from 1.4 GPa to 2 GPa[52–54] depending on the synthesis protocol; thus, 2 GPa for LPSCl can be regarded as the upper limit. In contrast, the oxyhalides examined in this study exhibit up to four-fold lower hardness ($H \leq 0.4$ GPa), consistent with previous reports on other chloride-based systems.[32] Although sulfides have been considered soft SEs because they can be densified at room temperature, the lower work of compression and microindentation hardness demonstrate that LMOCs, especially LAOC, can be considerably softer.

To evaluate the influence of stack pressure on the ionic conductivity, the SE pellets were first densified at 120 MPa for 3 minutes, followed by EIS measurements under progressively reduced stack pressures (Fig. 1f). A carbon foil was employed as a compliant interfacial layer to improve the contact between the current collector (CC) and the SE, which helps to reliably measure the ionic conductivity at low stack pressures (<5 MPa).[47] The corresponding Nyquist plots are shown in Fig. S6. Among all the electrolytes, LPSCl exhibits the most significant decrease in ionic conductivity (-56%) when the stack pressure is reduced from 55 to 7.2 MPa, which is consistent with the lack of densification. In contrast, LAOC shows only a minor reduction of -4% under the same unloading pressure conditions. This agrees well with the recent study by You *et al.* and is attributed to its softer and viscoplastic nature, which better accommodates interfacial deformation.[43] Meanwhile, LNOC and LTOC display a comparatively moderate decrease of -17% and -14%, respectively. The dependence of the ionic conductivity on pressure is most likely due to a high degree of densification and, therefore, less elastic relaxation upon unloading. In general, it is expected that materials with high work of compression (*i.e.*, LPSCl) will exhibit more elastic relaxation and less densification when removing the applied stress. This finding agrees well with the FIB-SEM and hardness measurements, where the oxyhalides show higher densification and lower resistance to plastic deformation compared to LPSCl. A decrease in the ionic conductivity with decreasing pressure for the oxyhalides follows the trend in the hardness and work of compression with LAOC $<$ LNOC $\approx$ LTOC.

Mesoscale modelling of densification and contact area evolution at the H-E interface

Mesoscale modelling techniques were used to understand (i) the pressure-induced densification of the LPSCl and LAOC SEs, and (ii) the evolution of the H-E contact fraction at the LPSCl|LLZTO and LMOC|LLZTO (M = Nb and Al) interfaces under different stack pressures. Creep is assumed to be the primary mechanism by which densification is achieved.[55] Higher pressures promote creep deformation that governs densification in softer SEs (such as sulfides and oxyhalides). It should be noted that for the purpose of modelling the densification behavior, the yield stress $\left(\sigma_y = \frac{H}{3}\right)$ is preferred over flow stress (σ_f) for LPSCl as the homologous temperature during densification at room temperature ($T_H < 0.4$), and it melts congruently at 532 °C.[56] Although σ_f may be more appropriate for LMOCs, it is difficult to define a melting point for LAOC due to its polymeric structure and for LNOC/LTOC due to its nanocrystalline-amorphous nature.[44]

The predicted model microstructures of the SEs were densified at 120 MPa for 3 minutes at room temperature under the same experimental conditions in the section above, considering different σ_y. The microstructures are shown in Fig. 2a. For the case where the yield strength is larger than the applied pressure ($\sigma_y > P_{app}$), less deformation occurs, resulting in a lower relative density compared to when ($\sigma_y < P_{app}$).[57,58] Creep-induced densification at lower temperatures is particularly important for soft electrolytes, such as LMOCs, if sufficient pressure is applied to exceed their σ_y. The mesoscale model-predicted evolution of relative density with time under an applied pressure of 120 MPa, with and without creep deformation, is shown in Fig. 2b. For materials with lower σ_y (such as LAOC, red trace), it is possible to obtain almost 100% relative density within 30 seconds due to the presence of the creep deformation-induced densification (see red trace in Fig. 2b). However, materials with higher σ_y (such as LPSCl) demonstrate limited creep-induced densification at 120 MPa, which leads to minimal improvement in relative density, as shown by the green trace in Fig. 2b. The model-predicted trend in densification is in good agreement with the experimental observations, as depicted in Fig. 1a and c.

To better understand how fabrication pressure affects the evolution of interfacial contact at the H-E interface, a separate mesoscale level model was developed for studying the LPSCl|LLZTO, LNOC|LLZTO, and LAOC|LLZTO interfaces (Fig. 2c). The mesoscale model begins with a flat surface for the softer catholytes (LPSCl, LNOC, and LAOC) and a rough LLZTO surface with root mean square roughness, *Sq*, of $\sim$220 nm, to simulate the pellet-to-pellet configuration. The evolution of interfacial contact with increasing pressure at

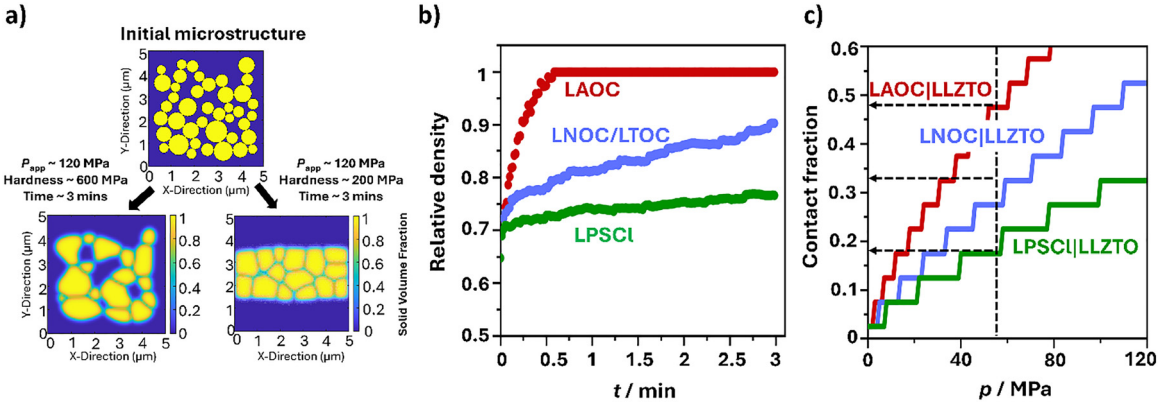

Fig. 2 (a) Evolution of the particle microstructure during the densification of LPSCl (left) and LAOC (right) SEs under 120 MPa and room temperature, but with different hardness values. (b) Increase in the relative density with time under an external pressure of 120 MPa for LPSCl (green), LNOC/LTOC (blue) and LAOC (red). (c) Increasing contact fraction of the LMOC|LLZTO H-E interface across different stack pressures.

room temperature was then analyzed. This configuration was selected to reflect the assembly conditions of the full cells fabricated in this study, as the powder-to-pellet method for densifying LMOCs on LLZTO resulted in lower Coulombic efficiency (~98%), as discussed later. The deformed configuration of the LPSCl|LLZTO, LNOC|LLZTO, and LAOC|LLZTO interfaces at similar stack pressures (*i.e.*, 55 MPa) used for the bilayer symmetric cells is demonstrated in Fig. 2c (dashed horizontal arrows). Under a pressure of 55 MPa, LPSCl, LNOC and LAOC demonstrate 17%, 28%, and 47% H-E contact fractions, respectively. In short, due to the higher σ_y and less creep deformation, achieving a similar contact fraction for LPSCl|LLZTO and LNOC|LLZTO requires a higher fabrication pressure. The model-predicted trends of the higher transfer-active contact area enabled by softer electrolytes correlate well with the resistance evolution in the low frequency (LF, *i.e.*, H-E) interface region, and its physical origin is discussed below.

Electrical properties of bilayer symmetric cells

The kinetics at the H-E interface are not solely governed by pore-induced geometric constriction at the anolyte|catholyte interface. They are also influenced by surface passivation layers (*e.g.*, LiOH and Li_2CO_3), which govern ionic transport between the contacted materials. Previous studies on sulfide|Al–LLZO, halide|LLZTO, and (polyethylene) oxide|LLZTO polymer systems have shown that the H-E interfacial resistance is highly sensitive to the surface chemistry of LLZTO.[33–35,59]

Fig. 3 compares the resistance and activation energy (E_a) values of LMOC|LLZTO|LMOC bilayer symmetric cells (see methods for cell fabrication, Scheme S1) extracted from their Nyquist plots. We identify three processes in the Nyquist plots arising from bulk (>3.0 MHz), grain boundary (50–80 kHz) and the H-E interface (3–6 kHz) (Fig. 3a and b) contributions. We note that "bulk" here refers to a superposition of the resistance of $LLZTO_{Bulk}$ and $LMOCs_{total}$, while grain boundary resistance refers only to $LLZTO_{GB}$. In the bilayer symmetric LMOC|LLZTO|LMOC (M = Nb and Ta) cells, the first two relaxation processes align well with those of the $LLZTO_{(Bulk+GB)}$[37,60] (Fig. S7a–c), as demonstrated more clearly by DRT analysis (Fig. 3d and e). Notably, the low-frequency (LF) contribution associated with the H-E interfacial resistance appears only in the bilayer symmetric cells (*i.e.*, LNOC and LTOC|LLZTO). Because the LLZTO surface was only mechanically polished, partial removal of the native passivation layer is expected. Thus, what is measured in the LF region in the LMOC|LLZTO|LMOC cells (M = Nb and Ta) is a contribution of a more complex interface consisting of LMOC|LLZTO and a passivation layer of Li_2CO_3/LiOH on the LLZTO (which is always present). Surface roughness analyses of Li_6PS_5Cl|Al-LLZO and $Li_7P_3S_{11}$|Al-LLZO interfaces confirmed that geometric constriction dominates the overall resistance, with increasing roughness shifting the average time constant of the H-E interface to lower values across all temperatures (−40 °C to +40 °C).[33,35] A similar trend was observed here: mechanical polishing (MP) of LLZTO pellets inside an Ar glovebox significantly affected the interfacial behavior (Fig. S8a–c). Rougher LLZTO surfaces (P400 grit, $Sq \approx 300$ nm) exhibited lower H-E resistance than fine polished ones (P4000 grit, $Sq \approx 30$ nm) (Fig. S8a) likely due to increased transfer-active contact area.[61,62] Converting the individual resistances in the time domain by performing distribution of relaxation times (DRT) analysis reveals that the interfacial contribution was prominent for fine-polished LLZTO but nearly absent for rougher surfaces (Fig. S8b). Consequently, a medium surface finish (P1000 grit, Sq = 120–150 nm) was adopted, providing a distinct H-E interface resistance and consistent deconvolution across all temperature ranges used for time constant and activation energy analysis of bilayer symmetric cells.

The H-E resistance and the corresponding capacitance values at 55 MPa and 25 °C for the LNOC|LLZTO|LNOC and LTOC|LLZTO|LTOC bilayer symmetric cells are (150 ± 24) Ω cm^2 and (3.6 ± 0.1) μF cm^{-2}, and (155 ± 10) Ω cm^2 and (2 ± 0.2) μF cm^{-2}, respectively, while the H-E resistance for the LAOC|LLZTO|LAOC cells is significantly smaller (35 ± 5) Ω cm^2, and the capacitance is larger (7 ± 2) μF cm^{-2}. The value of resistance is doubled while the capacitance value is halved since two interfaces are measured in a

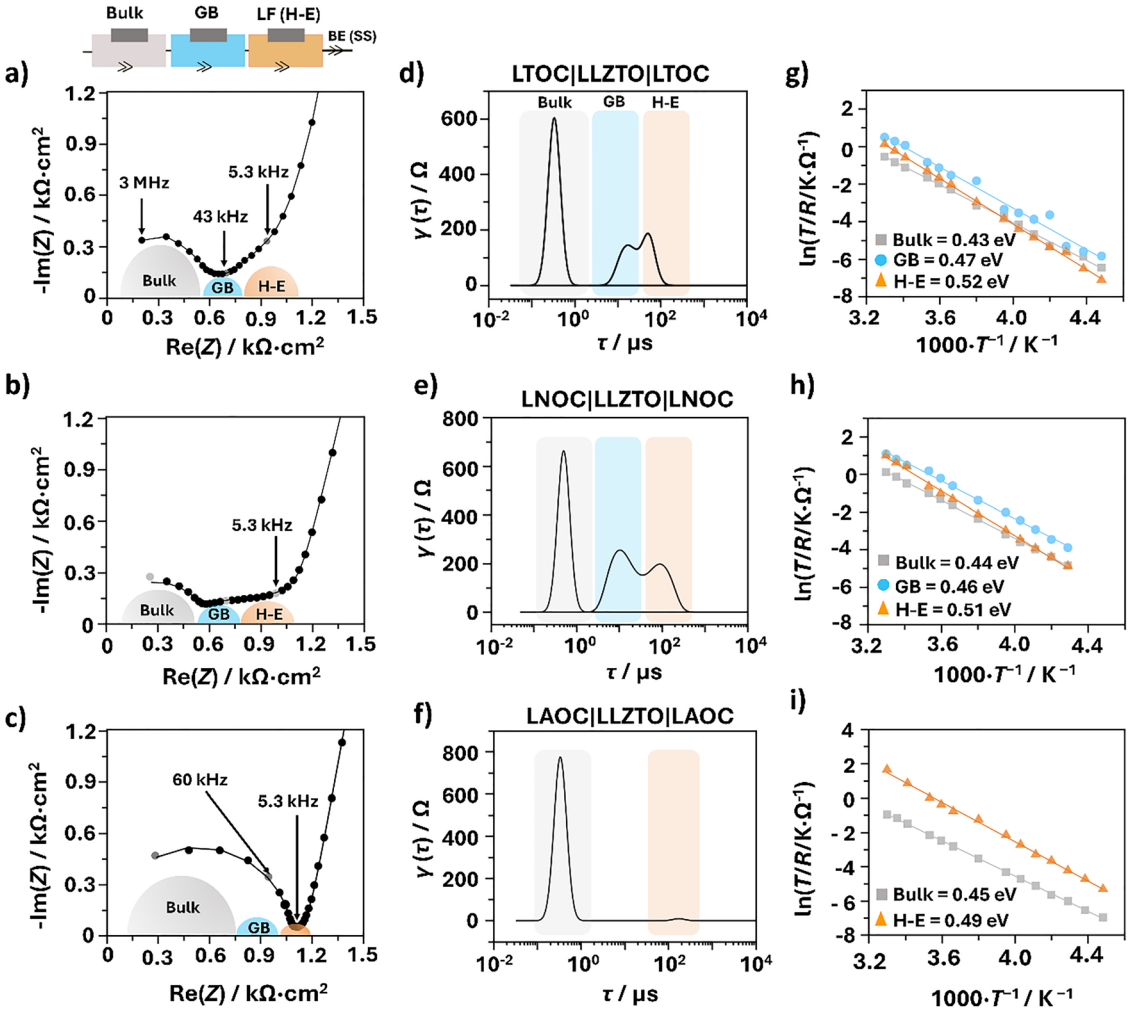

Fig. 3 Nyquist plots collected at 55 MPa and 25 °C for the bilayer symmetric LMOC|LLZTO|LMOC cells: (a) LTOC, (b) LNOC, (c) LAOC, and (d)–(f) the corresponding DRT maps. The hetero-electrolyte contribution observed at the lower frequency range (LF ≈ 5 kHz) is denoted in orange; with the corresponding Arrhenius plots for (g) LTOC and (h) LNOC describing the activation energies for the bulk (HF), GB (MF) and H-E contributions, and (i) LAOC showing only the bulk (HF) and H-E (LF) contributions.

symmetric cell setup, as discussed above. The trend in these values agrees well with that from the FIB-SEM, the work of compression, microindentation hardness measurements, and ionic conductivity relaxation, as illustrated in Fig. 1. LTOC and LNOC have nearly identical mechanical behavior that corresponds to similar H-E resistances and capacitances, while the softer mechanical properties of LAOC correspond to a lower resistance and higher transfer-active contact area at the H-E interface, as indicated by the larger capacitance values than those of the LNOC and LTOC|LLZTO cells. Notably, in the LAOC|LLZTO|LAOC configuration (Fig. 3c), the grain-boundary contribution could not be resolved likely due to similar characteristic frequencies of bulk transport in LAOC (~70 kHz) and the LLZTO grain boundary charge-transfer (~60 kHz), and the H-E interface resistance is almost negligible, as confirmed from the DRT analysis (Fig. 3f).

Further corroboration is provided by the comparison of temperature-dependent impedance measurements to measure the respective E_a and τ values of different processes under equilibrium conditions (*i.e.*, no current load).[33,35,37] For the bilayer symmetric cells, LTOC|LLZTO|LTOC and LNOC|LLZTO|LNOC configurations were investigated in this study; the E_a values observed were 0.43 eV for the high-frequency (HF) region, 0.48 eV for the mid-frequency (MF) region and 0.51 eV for the low-frequency (LF) or H-E interface region (Fig. 3g and h). The first two energies closely match those of the HF and MF values from $LLZTO_{(Bulk+GB)}$ (Fig. S2). These activation energies are much higher than those of the respective LNOC and LTOC ($E_a \approx 0.29$ and 0.24 eV, respectively), indicating that the contribution is dominated by the LLZTO solid electrolyte with the highest E_a for the H-E interface, especially for LNOC and LTOC|LLZTO bilayer symmetric cells (Fig. S9). As noted above, the LAOC|LLZTO|LAOC cell exhibits two distinct processes corresponding to bulk transport and H-E interface, with E_a values of 0.45 eV and 0.49 eV, respectively (Fig. 3i). The H-E interfacial E_a closely matches the grain-boundary E_a of LLZTO, suggesting that the H-E interface behaves similarly to the grain

boundary once the geometric current constriction is removed. As reported by Eckhardt and Kremer *et al.*, the largest potential drop occurs across the lower-conductivity electrolyte layer, thereby dominating geometric current constriction.[37] In this case, LLZTO and LAOC possess almost comparable ionic conductivity, and the overall resistance is dominated by the bulk transport of the respective SE layer.

The average resistance values obtained from triplicate cells are summarized in Table S2, and the corresponding Nyquist plots recorded at −40 °C and 55 MPa are presented in Fig. S10. The temperature dependent τ (Fig. S11) of the HF and MF components are comparable to those of bulk transport in LLZTO and grain boundary charge transfer of LLZTO, respectively, while the H-E interface (or LF contribution) has the highest average τ and lowest characteristic frequency, as they correlate with the relaxation time constant (Fig. S11). This low characteristic frequency is attributed to the geometric constriction effects that may arise from pores and passivation layers commonly associated with H-E interfaces.[36] If full contact at the H-E interface was achieved (*i.e.*, LAOC|LLZTO cell), its characteristic frequency would instead be closer to the MF region, similar to a grain boundary (or MF) process (*i.e.*, LAOC|LLZTO cell). This demonstrates that the H-E interface leads to a significant potential drop in dual electrolyte cells.

Effect of passivation layers on charge transfer across the hetero-electrolyte interface

Although it is well known that the surface chemistry of LLZTO impacts the charge transfer kinetics at the interface with Li metal, the hetero-electrolyte interface has been considerably less studied.[33–35,63,64] To quantitatively analyze the chemical components and optimize the surface chemistry of LLZTO pellets, both dry (heat treatment, HT) and wet (phosphoric acid treatment, H_3PO_4) methods were used to evaluate the effectiveness of the H-E interface between the LLZTO and LMOCs (see methods for details on surface treatment of LLZTO pellets: SI).

The LNOC|LLZTO|LNOC bilayer symmetric cell was selected as a case study to examine the effect of removing the passivation layers on LLZTO. LNOC was chosen because it had the most discernible H-E resistance (Fig. 3b) that is evident in the low frequency region in the DRT analysis (Fig. 3e), and LNOC is a more well-understood material in the literature.[44,65–67] At the same mechanical polish finish (P1000 grit, Sq = 120–150 nm), the H-E interface resistance after HT and H_3PO_4 treatment was (37 ± 25) and (41 ± 15) Ω cm^2, respectively (Fig. 4a and Fig. S12). There was a greater variability in the LMOC|LLZTO$_{HT}$ cells noted by the large error bars, indicating that this procedure is less reproducible. This could be due to the reoccurrence of passivation layers even under Ar glovebox-like conditions, as reported previously by Siniscalchi *et al.*[68] After H_3PO_4 treatment, the H-E interface resistance was mainly consistent and more reproducible (Fig. 4b). The reduced H-E resistance after the H_3PO_4 treatment may come from increased surface roughness induced by acid etching, as reported previously.[34] This surface modification likely enhances the transfer-active contact area at the LLZTO|LMOC interface, thereby facilitating ion transfer.[33,35] Furthermore, the E_a values after HT treatment (0.49 ± 0.01) eV were slightly lower than those of LLZTO$_{MP}$ (0.51 ± 0.01) eV (Fig. 4c and Fig. S12b). In contrast, slightly higher E_a (0.54 ± 0.01) eV (Fig. 4c and Fig. S12d) was observed for H_3PO_4-treated LLZTO discs (discussed below).

The X-ray photoelectron spectroscopy (XPS) analysis of the LLZTO pellets after various surface treatments is shown in Fig. 4d(i–iv) and Fig. S13, and their respective H-E resistance and E_a values are summarized in Table S3 to clarify the surface chemistry effects. The presence of a passivating Li_2CO_3 contamination layer with a thickness greater than the penetration depth of the X-ray (~5–10 nm) is evident in the O 1s spectra corresponding to the pristine LLZTO, which obscures the underlying signal from the lattice oxygen of the garnet at ~528.9 eV.[68,69] The O 1s spectra of LLZTO$_{MP}$ and LLZTO$_{HT}$ reveal three major peaks, which are assigned to Li_2CO_3 (531.6 eV), LiOH (530.7 eV) and LLZTO lattice oxygen (528.9 eV).[69,70] Both MP and HT remove Li_2CO_3/LiOH although the HT cleans the LLZTO more effectively, as evidenced by the larger lattice oxygen signal. The more efficient removal of the Li_2CO_3/LiOH from the LLZTO$_{HT}$ surface leads to a lower E_a compared to the LLZTO$_{MP}$. Li_2CO_3 and LiOH are also present on the H_3PO_4-treated LLZTO, along with a PO_4^{3-} signal (531.5 eV) that overlaps with the Li_2CO_3.[71] It is known that the H_3PO_4 treatment of LLZTO phosphorylates the metal (Li, La, and Zr) ions, forming a phosphate layer.[69,71] The lattice oxygen signal is less prominent compared to the LLZTO$_{MP}$ due to the metal phosphate layer consuming the bulk LLZTO signal and not due to Li_2CO_3/LiOH contamination. The metal phosphate layer also likely causes higher E_a. Thus, the HT, MP, and H_3PO_4 methods are effective in removing passivation layers on the surface of LLZTO, which is consistent with previous reports.[69]

To evaluate the impact of low stack pressure on the optimized LLZTO$_{HT}$ surface, symmetric cells were assembled using the powder-to-pellet method, as previously described. The resulting effective stack pressure ranged from 1.8 to 8.2 MPa. The Nyquist plots obtained at a pressure of 1.8 MPa for bilayer symmetric LMOC|LLZTO|LMOC cells (Fig. S14) each clearly show the three contributions: the bulk SEs, grain boundaries of LLZTO and the H-E interface. The H-E resistance extracted from the fitting is presented in Fig. 4e for LAOC (e-*i*), LTOC (e-*ii*) and LNOC (e-*iii*), respectively, along with the corresponding capacitance values. As the pressure increases, a clear decrease in H-E interface resistance and an increase in capacitance were observed for all three SEs, which can be attributed to geometric current constriction effects, as previously reported.[37,72] At the lowest stack pressure of 1.8 MPa, the H-E resistance values for LNOC and LTOC ((250 ± 30) and (270 ± 30) Ω cm^2, respectively) are almost double that of LAOC (150 ± 30 Ω cm^2) owing to the lower hardness of the latter. As mentioned, geometric current constriction resistance at the H-E interface dominates at low stack pressures and is affected by the ionic conductivity of the electrolytes (*i.e.*, higher ionic conductivity yields lower constriction resistance).[37,38] Even though LAOC has an order of magnitude lower ionic conductivity than LNOC and LTOC, the H-E resistance is at least 40% lower. We believe that this is a

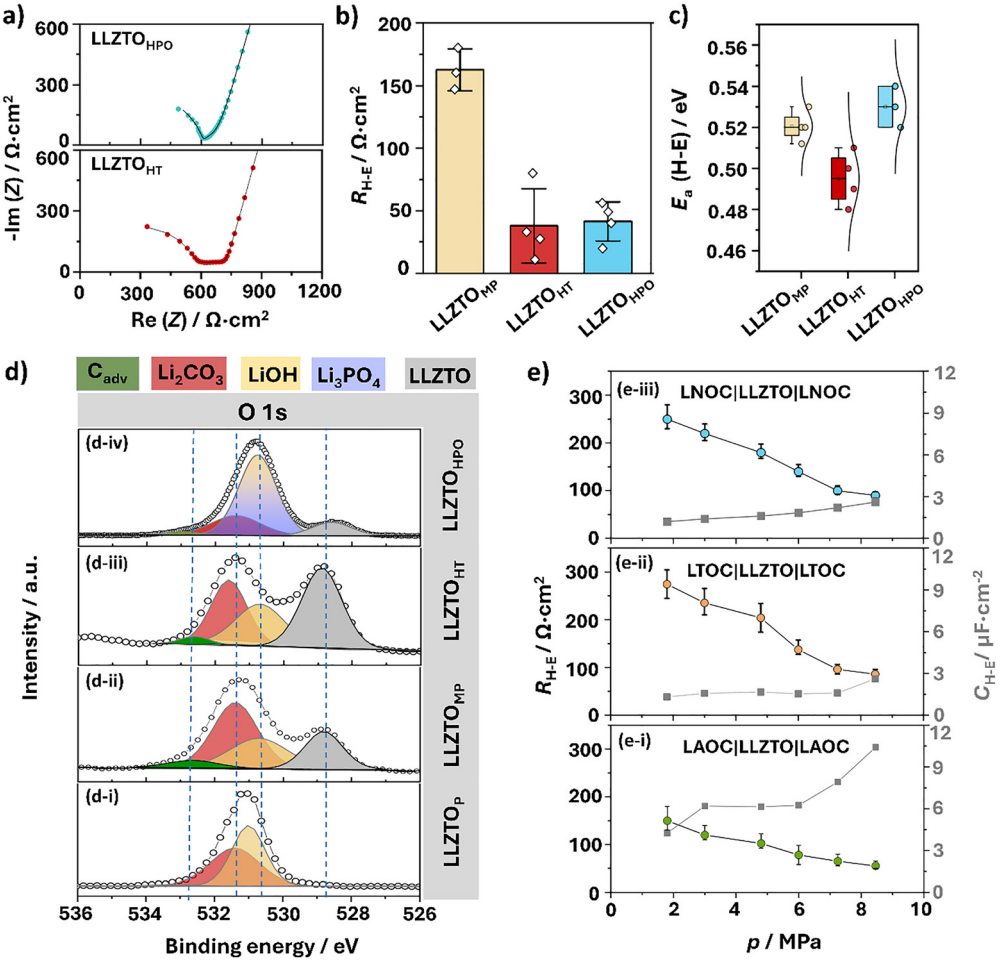

Fig. 4 Comparison of the Nyquist plots of the bilayer symmetric cell (a) SS|LNOC|LLZTO|LNOC|SS at 25 °C and 55 MPa stack pressure after phosphoric acid (H_3PO_4) and heat treatment (HT). Comparative analysis of the (b) hetero-electrolyte resistance and (c) activation energies (E_a) after mechanical polishing (LLZTO-MP), heat treatment (LLZTO-HT) and phosphoric acid (LLZTO-HPO) treatment. (d) XPS analysis of O 1s spectra of (LLZTO-Pristine), (LLZTO-MP), LLZTO (HT), and LLZTO (HPO). (e) Comparison of the H-E interface of bilayer symmetric cells of C|LNOC|LLZTO|LNOC|C, C|LTOC|LLZTO|LTOC|C and C|LAOC|LLZTO|LAOC|C. The bar plots consist of standard deviation with at least 3 cells. The lines are a guide to the reader in (e).

significant reduction in interfacial resistance at low stack pressures. Thus, the mechanical properties have a larger influence on the H-E resistance than the ionic conductivity for inorganic H-E interfaces. Previous studies on the LPSCl|LLZO H-E resistance reported an H-E resistance of 9368 Ω cm^2 at 1 MPa and ~175 Ω cm^2 at 30 MPa.[35,39] This further emphasizes the benefits of softer LMOC electrolytes. At 6 MPa, close to the pressures used to run full cells (discussed below), the H-E resistance for LNOC was less than 100 Ω cm^2 and even lower for LAOC, which is promising for practical applications. The H-E interfacial capacitance at 6 MPa observed for the LMOC|LLZTO (M = Nb and Ta) cell (2.2, 1.6 μF cm^{-2}) was lower compared with that of the LAOC|LLZTO cell (6 μF cm^{-2}). This confirms that the larger transfer-active contact area in the latter remains at low stack pressures (Fig. 4e).

Full cell performance with the LMOC|LLZTO dual electrolyte

After demonstrating a low and stable resistance at the LMOC|LLZTO interface, a dual electrolyte LLZTO and LNOC full cell was assembled. LNOC was chosen over LAOC and LTOC as it has the highest ionic conductivity, making it a more suitable catholyte, despite its less favorable H-E interface properties. Initially, full cells were attempted following the powder-to-pellet method, as discussed above, by densifying an LNOC interlayer and composite cathode against LLZTO at 120 MPa. Full cells fabricated using this procedure exhibited a low Coulombic efficiency (~98%) and were often shorted (Fig. S15). The low fabrication pressure likely leads to poor cathode density, limiting performance. An alternative procedure is to pre-densify the LNOC and composite cathode separately at higher fabrication pressures and then integrate them together in an Li|LLZTO half-cell (pellet-to-pellet method).[34] This enables higher composite cathode density and uniformity, although with the consequence of higher resistance from constriction at the LMOC|LLZTO hetero-electrolyte interface.[34] In each full cell, the LLZTO side in contact with the LNOC was treated with H_3PO_4 for better reproducibility, as shown in Fig. 4b, despite having a high activation energy barrier across the H-E interface. In any case, full cell performance does not depend on the LLZTO surface

treatment, *i.e.*, it is consistent with a heat-treated or H_3PO_4-treated LLZTO surface as discussed later. Thus, full cells built using the pre-densification method are tested at a stack pressure of 7 MPa at 60 °C to lower the constriction resistance (Fig. S16) at the H-E interface (see the Experimental for a detailed description of the cell assembly).

A full cell investigation was conducted using a composite cathode of NMC : LNOC in a ratio of 7 : 3 by weight. This corresponds to a volume fraction of 57% for NMC and 43% for LNOC, assuming their respective densities of 4.63 g cm^{-3} and 2.61 g cm^{-3}, respectively.[73] Only 20 mA h g^{-1} of capacity is attained due to poor electrical wiring within the composite (Fig. S17), while the expected capacity is >180 mA h g^{-1}. To alleviate this issue, vapor-grown carbon fibers (VGCFs) were added into the composite. It is known that carbon additives exacerbate the oxidation of solid electrolytes at high voltages.[74,75] Thus, to elucidate the effects of carbon on the stability of LNOC at a high state of charge (SOC), full cells were assembled with 2 wt% and 5 wt% VGCF while maintaining an NMC : LNOC ratio of 7 : 3 by weight (schematic, Fig. 5a). Each experiment was repeated at least in triplicate, with the values reported as the average. The cells were cycled once at a C/10 rate (assuming 1C = 200 mA g^{-1}) as an activation cycle (denoted as cycle 0; then, the current density was increased to C/5 in the range of 2.8–4.3 V *vs.* Li^+/Li.

The galvanostatic charge/discharge curves and performance of representative Li|LLZTO|LNOC|NMC cells are shown in Fig. 5b and c. The triplicate cycling data are presented in Fig. S18. During the activation cycle, the 2 wt% and 5 wt% cells demonstrate near full utilization of the NMC with a high initial discharge capacity of (186.4 ± 8.3) and (200.1 ± 17.1) mA h g^{-1}, respectively. The lower capacity in the 2 wt% cells is attributed to inhomogeneity in the mixing of the composite cathode.[76] As each cathode was not batch processed and instead was measured and hand mixed separately, a large variation from sample to sample was possible.[76] The 2 wt% cells exhibit less polarization during cycling compared to the 5 wt% VGCF cell (Fig. 5b). After 25 cycles, the 2 wt% cells retain 92.6% ± 2.9% of the initial capacity while the 5 wt% cell retains only 85.0% ± 1.0% (Fig. 5c), indicating more capacity deterioration as a result of LNOC degradation with higher VGCF content.

To investigate the cause of the VGCF effects on the capacity, EIS was carried out after the activation cycle and then every 5 cycles. EIS was performed at 100% SOC. Representative Nyquist plots of the 2 wt% and 5 wt% cells in the charged state are shown in Fig. 5d and e, respectively. The Nyquist plots were not normalized by electrode area, as the electroactive surface area in the composite cathode is not known. The Ohmic resistance in the cells originates from the bulk conduction in LLZTO and the LNOC interlayer, although at 60 °C, the time constants for

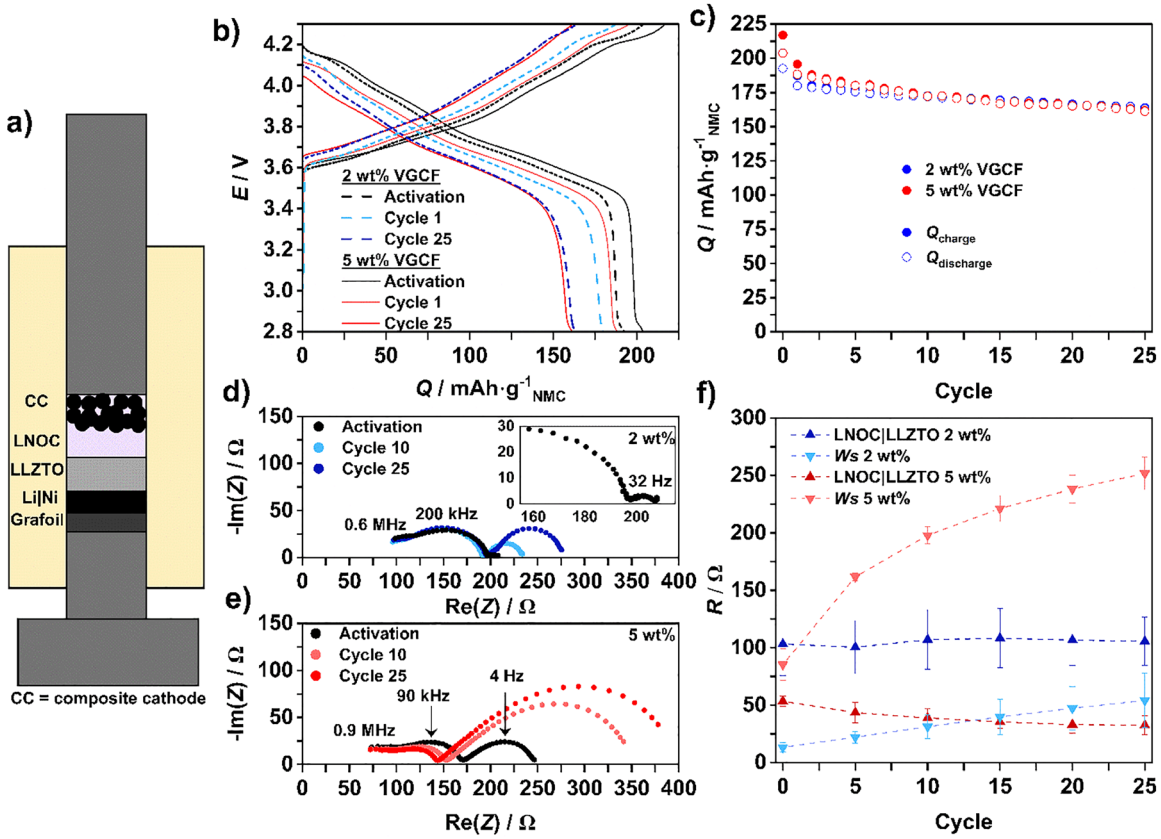

Fig. 5 (a) Cell schematic of a dual electrolyte battery. (b) Charge and discharge curves of the 2 wt% (blue) and 5 wt% (red) full cells. The voltage is referenced to Li^+/Li. (c) Charge/discharge capacity of the full cells. Nyquist plot in the charged state of the (d) 2 wt% full cell and (e) 5 wt% full cell. (f) LNOC|LLZTO interface and low-frequency semicircle (*Ws*) for the full cells. The dashed lines are guidance to the eye of the reader.

the bulk transport properties are too short to be probed using a maximum of 7 MHz frequency. The HF semicircle (0.6–0.9 MHz) is attributed to the grain boundary resistance in the LLZTO, while the MF semicircle (90–200 kHz) is attributed to the LNOC|LLZTO interface. The increase in the characteristic frequencies compared to those depicted in Fig. 3 is due to the increased temperature, which lowers the overall resistance and time constant. At very low frequencies (<50 Hz), where diffusion processes often dominate, we observe that a 45° line transitions into a semicircle. This behavior in EIS is characteristic of finite diffusion with a transmissive boundary. This process can be described by a short Warburg element, *W*s. Longer diffusion lengths through an increasing interphase growth or increased tortuosity lead to a larger resistance at low frequencies. This is precisely what is observed for the 5 wt% VGCF content compared to 2 wt%. As expected, a higher VGCF content increases the ''electrical wiring'' of the LNOC, which results in greater interphase growth owing to the oxidation of the electrolyte at high potential, thus increasing resistance, which is detrimental to long-term performance. Furthermore, the *W*s element naturally arises in mixed ionic-electronic conductors, such as a composite cathode.[77] To quantify the changes in the resistance, the charged Nyquist plots were fit with an *R*(*RQ*)(*RQ*)(*W*s) equivalent circuit model. This model fits the data well and is shown in Fig. S19 instead of Fig. 5 for clarity. The resistance of the LNOC|LLZTO interface does not increase in either cell during cycling (Fig. 5e) and remains $<100\ \Omega\ cm^2$, demonstrating the (electro)chemical stability of the LMOC|LLZTO interface. To further demonstrate that the elevated temperature used during cell cycling does not contribute to an increase in the H-E interfacial resistance, Nyquist plots of bilayer symmetric cells (LMOC|LLZTO, M = Nb and Al) were recorded at room temperature before and after heating the cells to 60 °C, followed by re-equilibration at room temperature (Fig. S20a and b). No significant changes in the impedance response were observed, indicating that thermal exposure does not induce additional interfacial resistance. Long-term stability measurements of the LNOC|LLZTO interface at 60 °C for 300 h (Fig. S28c) show a stable impedance profile, suggesting that no detectable side reactions occur between the two solid electrolytes under these conditions. The LMOC|LLZTO stability agrees with previous studies showing better stability at the LMOC|LLZTO interface compared to the LLZTO|sulfide interface. On the contrary, in the 5 wt% cells, the process described by *W*s grows from a resistance of $(85.4 \pm 13.5)\ \Omega$ after the activation cycle to $(251.6 \pm 14.2)\ \Omega$ after the 25th cycle. The *W*s resistance is significantly smaller in the 2 wt% cells, with a resistance of $(13.2 \pm 4.1)\ \Omega$ after the activation cycle. Although the *W*s grows during cycling, the resistance remains below the initial resistance of the 5 wt% cell at $(54.1 \pm 23)\ \Omega$. Hence, 5 wt% VGCF is not necessary to electrically wire the composite cathode completely, and the excess VGCF is detrimental to long-term performance by increasing resistance and causing a larger capacity fade. Further investigation into the origin of the *W*s process and the degradation of the cell is discussed later.

Ag interlayer for Li reservoir-free batteries

Next, the effects of stack pressure on the full cell were studied with 2 wt% VGCF. A full cell was cycled at 7 MPa; then, the pressure dropped to 5 MPa, 3 MPa, and finally to 1 MPa. This study was attempted with a thin Li foil anode, although abnormal discharge curves indicated poor stripping behavior at 1 MPa. To overcome these shortcomings, the Li foil was replaced with an *in situ*-formed Li anode improved using a silver interlayer for two reasons. First, an interlayer of silver (Ag) or gold (Au) has been shown to improve the performance of an *in situ*-formed Li anode at lower pressures.[75] Second, a Li reservoir-free cell allows for accurate Coulombic efficiency measurements because there is no ''infinite'' Li reservoir. Here, the Ag was sputtered onto the LLZTO; then, the LLZTO|Ag assembly was heat-treated at 400 °C in an Ar-filled glove box. After the heat treatment, de-wetting of the Ag occurs and forms discrete seeds uniformly distributed across the LLZTO surface (Fig. 6a). A similar de-wetting between LLZTO and Au was reported by Haslam *et al.*[78] Fig. 6a shows variation in the size of the Ag seeds, with a majority of the seeds <1 μm in diameter and a few larger seeds with a diameter between 1 and 5.5 μm. This seeded surface morphology was hypothesized by Haslam *et al.* to improve contact between seeded Au and the current collector to enable stable Li plating. Other studies have investigated the performance of flat Ag, but not *ex situ* seeded Ag.[79–81] Hence, the performance of the Ag seeds was characterized in a Li|LLZTO|Ag half-cell to confirm their viability as an anode interlayer. The Li|LLZTO|Ag half-cells were cycled under identical conditions to the full cell (*i.e.*, 7 MPa, 60 °C, and 2 mA h cm^{-2} capacity) with one activation cycle at a C/10 rate. To investigate the performance at different pressures, the half-cell was cycled 5 times at 7 MPa; then, the pressure was dropped to 5 MPa, 3 MPa, and 1 MPa with 5 cycles at each pressure. The activation of Li plating is shown in Fig. 6b. Several plateaus can be observed and are attributed to Li–Ag alloying (Fig. S21).[79,80]

During stripping, the overpotential remains stable up to at least ~90% depth of discharge (DoD) at each pressure (Fig. 6c) as determined by an inflection point in the voltage curve. Thus, the Ag seeds can enable the stable stripping of 2 mA h cm^{-2} from a thick *in situ*-formed Li anode at a pressure as low as 1 MPa if the discharge is limited to 90% DoD. Fig. 6d shows the Coulombic efficiency (CE) at each pressure when stripped to 100% DoD. The Ag seeds yield a CE of 97.35% in the activation cycle. This increases to 99.66% by the 2nd cycle at 7 MPa. Interestingly, the CE at the slower C/10 rate of the activation cycle is lower than that when stripped at C/5, which is attributed to the faster kinetics in a Li-rich Li–Ag alloy.[82] Further discussion is in the SI. Relatively high average CEs of 99.67% and 99.42% are maintained at 5 MPa and 3 MPa, respectively. The CE drops to ~97.61% and has a larger variance at 1 MPa, indicating poorer stripping capabilities. Nevertheless, this is one of the highest reported CEs for the solid-state Li–Ag interlayer system.[80] Furthermore, above 3 MPa, the CE approaches that of the full cell (CE ~99.55%). Therefore, the Ag interlayer is unlikely to be the limiting factor in full-cell performance under these conditions.

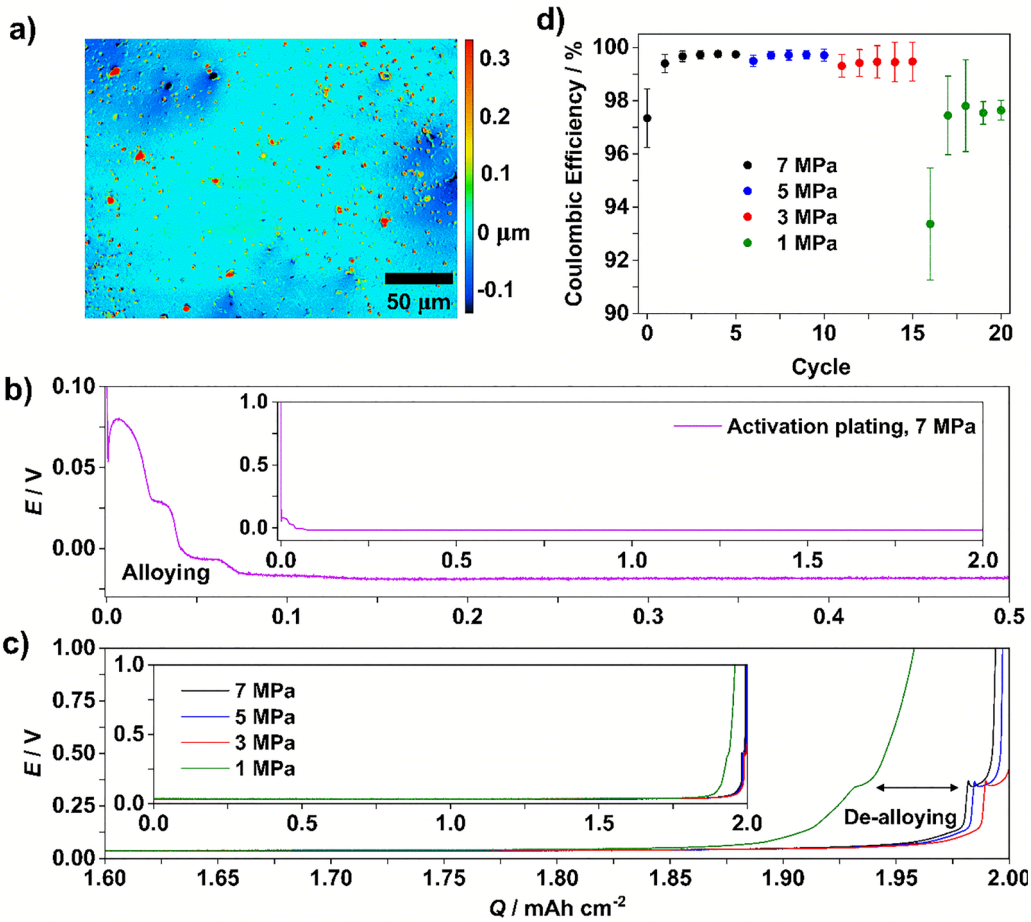

Fig. 6 (a) Laser confocal height map of the heat-treated silver (Ag) on LLZTO demonstrating the height of the Ag seeds. (b) First plating of Li to Ag during the activation cycle. Inset: The full plating profile. (c) Last stripping at each pressure at C/5. Inset: The full stripping profile. (d) Coulombic efficiency of each cycle with one standard deviation. The voltage is referenced to Li^+/Li.

SEM was utilized to investigate the morphology of the Ag in the discharged state after cycling. Fig. S22 shows the micron-sized structures covering the LLZTO surface. Ko *et al.* observed a similarly shaped microstructure when plating Li into Ag although the structures were <200 nm in size.[79] Energy dispersive X-ray spectroscopy (EDX) (Fig. S22b–d) confirms that these regions are rich in Ag. As Li and Ag form a solid solution, the Ag is likely dissolved and dispersed in the plated Li.[83–85] During stripping, the silver likely precipitates out of the shrinking *in situ* Li anode and redeposits onto the LLZTO surface.[80] The redeposited Ag strongly adheres to the LLZTO surface. Upon removing the current collector, the Ag remained adhered to the LLZTO. Similarly, the redeposited Ag could only be removed from the LLZTO by scratching with a razor blade, further demonstrating strong adhesion. This adhesion and redeposition onto the LLZTO surface in a similar distribution and size.

Li reservoir-free full cell

After confirming the viability of Ag seeds as an anode interlayer, Ag was incorporated into Li reservoir-free full cells. The Li reservoir-free cells were activated at C/10 and 7 MPa and then cycled 5 times at 7 MPa, followed by lowering the stack pressure to 5 MPa, 3 MPa, and then 1 MPa. A representative full cell is shown in Fig. 7a. A Li reservoir-free full cell with a heat-treated LLZTO surface (Fig. S18c) shows identical performance to the H_3PO_4-treated LLZTO. The alloying plateaus of Ag are noticeable within the first 6 mA h g^{-1} of the activation charge shown in the inset of Fig. 7a. The Li reservoir-free cells have a high activation discharge capacity of (203.2 $\pm$ 4.5) mA h g^{-1}. This high discharge capacity is comparable to the Li reservoir-free silver-carbon layer reported by Lee *et al.*[86] The activation cycle CE is 94.08% $\pm$ 0.06%, and at the end of discharge, no de-alloying plateaus are observed. This implies that the polarization of the Ag is minimal and remains in the flat Ohmic region described in the previous section. Thus, polarization in the cell is dominated by the NMC and demonstrates that Ag is not limiting. After the first two cycles, the cells have a high average CE of 99.57% across all pressures. This agrees well with the CE above 3 MPa in Li|LLZTO|Ag half-cell characterization. Interestingly, at 1 MPa, the full cell delivers a higher CE than the half-cell. This may be due to more Li lost in the full cell compared to the half-cell, yielding a more Li-rich Li–Ag interlayer. The cells maintain a high capacity and a consistent fade

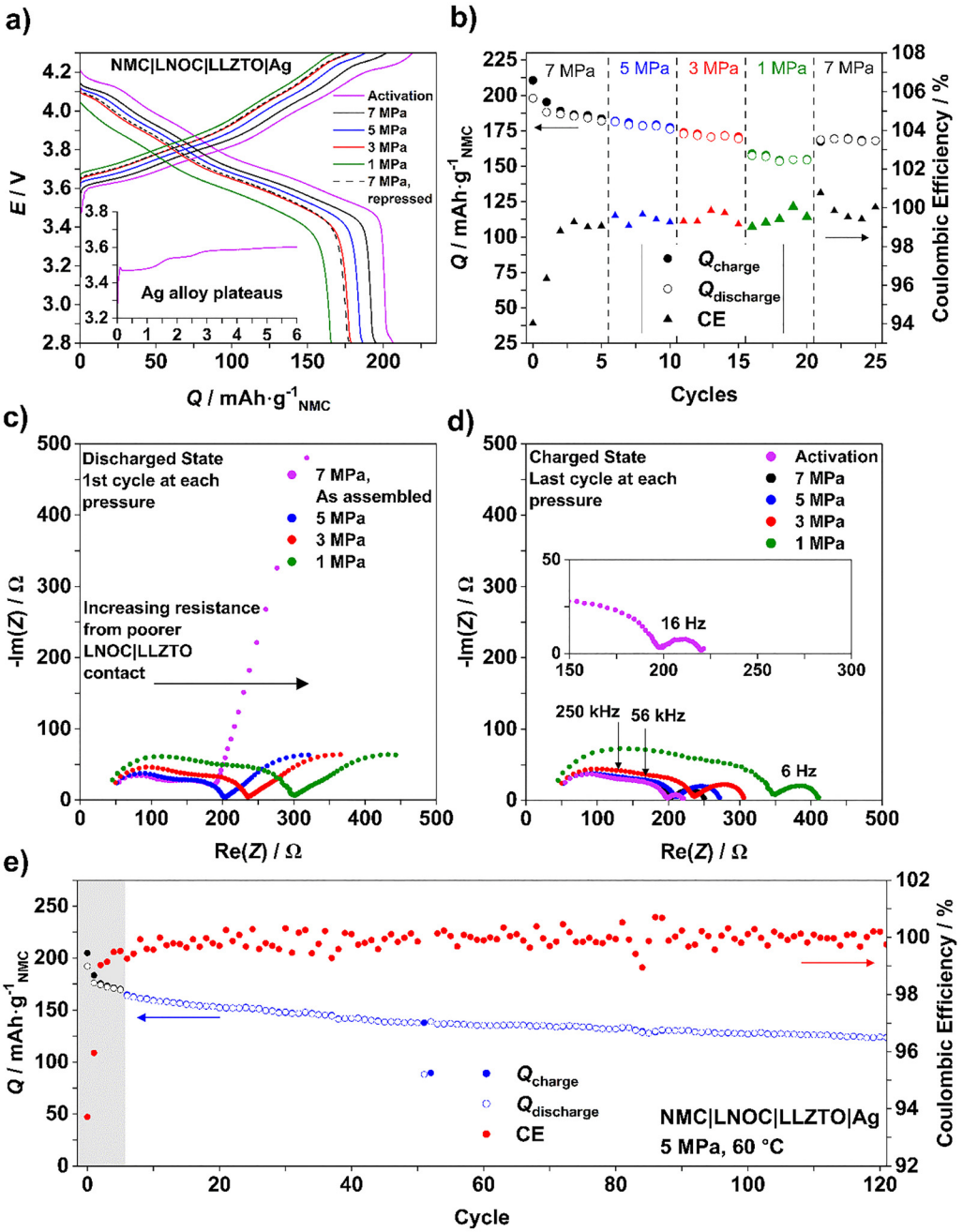

Fig. 7 Cycling data for an NMC|LNOC|LLZTO|Ag Li-reservoir-free full cell with an areal loading (~2 mA h cm^{-2}). (a) First charge/discharge curve at each pressure. Inset: Magnification of the activation cycle highlighting the Li-Ag alloying plateaus. (b) Capacity and Coulombic efficiency at different pressures. (c) Nyquist plots in the discharged state prior to cycling at each pressure. (d) Nyquist plots of the last cycle at each pressure in the charged state. Inset: Magnification showing the low frequency part of the activation plot. (e) Extended cycling of an NMC|LNOC|LLZTO|Ag Li-reservoir-free full cell (~2 mA h cm^{-2}). The activation and first 5 cycles were performed at 7 MPa (gray box). The drop in capacity near the 51st cycle was due to a connection issue.

down to 3 MPa (Fig. 7b). By decreasing the pressure to 1 MPa, the cells began to fade faster. Further studies need to be carried out to investigate full cell performance at lower current densities to separate the anode and cathode contributions to the capacity fade.

Representative Nyquist plots of a full cell at each pressure are shown in Fig. 7c. It can be observed from the Nyquist plots that total cell resistance increases upon lowering the pressure due to the increase in higher resistances. Previous studies have shown that constriction resistance at the LLZTO|halide and LLZTO|sulfide interface increases when lowering the stack pressure.[33–35] The individual resistance contributions from LLZTO and the LNOC|LLZTO interface are shown in Fig. S23. There is a negligible change in the LLZTO and LNOC|LLZTO resistance by decreasing the pressure from 7 to 5 MPa, a small change at 3 MPa, and a significant change at 1 MPa.

The increase in the LLZTO resistance is due to the loss of contact at the LNOC|LLZTO interface and current collector|-cathode interface.[34,87] With an increase in cell resistance, a larger overpotential when cycling exists, which leads to premature cell polarization. Thus, the capacity at lower stack pressures, especially at 1 MPa, is limited by the LNOC|LLZTO interface. Nevertheless, at 1 MPa, the cells still deliver a capacity of (157.6 ± 8.0) mA h g^{-1} on the 16th cycle. This demonstrates that while the LNOC|LLZTO interface remains stable during cycling, the initial resistance from constriction currently remains a challenge at low pressures (*i.e.*, 1 MPa) for LNOC|LLZTO dual electrolyte SSBs, as the original Ag seeds allow for high CE and stable cycling.

Fig. 7d shows the Nyquist plots of the charged cells during the last cycle at each pressure. The LF resistance continues to grow during cycling, as expected, although there appears to be no pressure dependence (Fig. S24). From 7 to 3 MPa, the LF resistance growth behavior is similar to that of the Li anode cell at 7 MPa (Fig. S24). However, the LF resistance drops unexpectedly at 1 MPa and then rebounds higher at 7 MPa. If lower pressures cause worse contact loss, it is expected that the resistance at 1 MPa will increase and not decrease. A decrease in cell resistance at lower pressures frequently indicates a soft short or dendrite. No voltage fluctuations in the charge/discharge curves indicate a soft short. To confirm that there are no dendrites, the LLZTO was removed after cycling (Fig. S25), showing both sides of the LLZTO. This confirms that no dendrites are the cause of the resistance decrease at 1 MPa. Furthermore, the LNOC interlayer remains white/tan. If there was Li penetration through the LLZTO, the LNOC would have turned black. In any case, a LNOC|LLZTO dual electrolyte enables high Coulombic efficiency of an *in situ* Li anode at 1 MPa. Fig. 7e confirms that Li reservoir-free cells can also operate at 5 MPa for longer cycling. Due to minimal resistance change from 7 to 5 MPa, longer term cycling was carried out at 5 MPa on one cell (Fig. 7e). The cell maintains a high Coulombic efficiency (~99.8% on average) with 70% capacity retention after 120 cycles.

Degradation characterization

Next, the cause of the resistance growth and capacity fading was investigated. A shortcoming of two-electrode full cells is the convoluted LF behavior of both the anode and cathode. Due to the difficulty of implementing a reference electrode into the cell, a Li|LLZTO|Li symmetric cell (Fig. S26) and an NMC|LNOC|NMC symmetric cell (Fig. S27) were assembled and characterized to deconvolute the LF processes in the Nyquist plot. To create an NMC|LNOC|NMC symmetric cell with a composite cathode at 100% SOC, a full cell was first assembled and charged to 4.3 V (Fig. S26a). The charged composite cathode was then incorporated into the NMC|LNOC|NMC symmetric cell, densified (Fig. S27b) and heated to 80 °C (Fig. S27c). The results shown in the SI confirm that the LF resistance is from the cathode.

To further characterize the parasitic reactions at high states of charge, a full cell with 5 wt% VGCF was assembled and charged to 4.3 V. Once at 4.3 V, the cell was rested under open circuit conditions, and EIS was conducted every 2 hours. Prior to charging, the cell was rested for 18 hours to determine if there were any parasitic reactions in the discharged state, as has recently been reported for Li_3InCl_6 and NMC.[88] The unchanged Nyquist plot in Fig. S20d confirms that at low

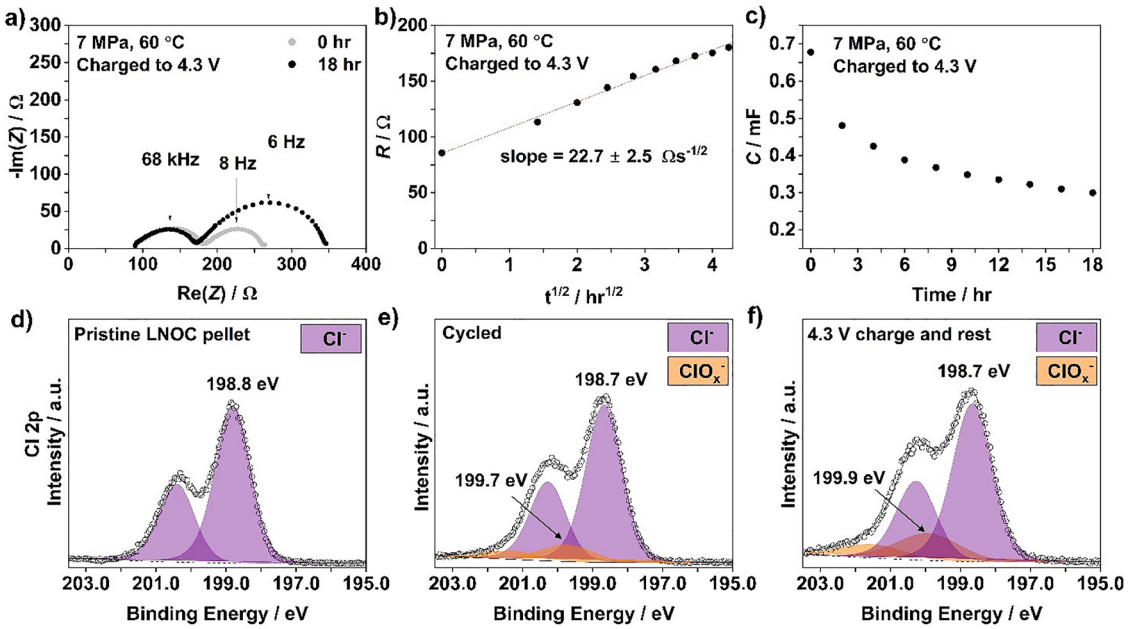

Fig. 8 (a) Time evolution Nyquist plots of a full cell charged to 4.3 V and rested at OCV. (b) Warburg resistance changing over time fit to a parabolic growth function. (c) Capacitance of the Warburg element over time from a). Cl 2p spectra of (d) pristine LNOC, (e) composite cathode cycled 25 times, and (f) composite cathode charged to 4.3 V and rested.

SOC, there are no reactions within the composite cathode. While resting at OCV after being charged to 4.3 V, the semicircle continues to grow over 18 hours, as shown in the Nyquist plot of Fig. 8a. This behavior was described for $Li_{10}GeP_2S_{12}$ (LGPS) and attributed to a diffusion-controlled cathode-electrolyte interphase (CEI).[9] Similar diffusion-controlled interphase growth was shown for the interface between various sulfides and Li.[26,75] The change in resistance over time is fit to a Wagner-type CEI growth model with resistance dependent on $t^{-1/2}$.[9,26] Fig. 8b shows a linear trend and fits the model well. From the model, the slope of the linear trend line, k', describes the CEI growth rate. Here, $k' = (22.7 \pm 2.5)\ \Omega\ h^{-1/2}$ at 60 °C. A higher temperature influences the rate constant by lowering resistance. Therefore, Zuo *et al.* introduced k'', the rate constant normalized to the initial resistance.[9] Here, $k'' = 0.536\ h^{-1/2}$ close to k'' of $\sim 0.5\ h^{-1/2}$ for the NMC|LGPS CEI at 40 °C. Thus, at high SOC, higher VGCF content exacerbates a parasitic reaction at the NMC|LNOC interface, which leads to faster cell degradation.

In the work on the NMC|LGPS interface, it was also shown that the CEI capacitance decreases parabolically over time. Fig. 8c shows the change in *W*s capacitance during the OCV rest, showing a parabolic curve, which agrees with the model. Interestingly, when analyzing the *W*s capacitance (Fig. S28) in the cycled full cell from Fig. 5, the capacitance does not decrease parabolically but instead increases parabolically. As the capacitance does not follow the expected trend, it can be concluded that at least two separate causes underlie the response of the LF capacitance. Currently, the explanation for the increase in capacitance is not well understood. To elucidate the (electro)chemical degradation of LNOC, XPS was performed on the composite cathodes cycled and charged to 4.3 V and rested. In the Cl 2p spectrum, pristine LNOC shows one peak at 198.8 eV and is assigned to Cl $2p_{3/2}$ from bulk LNOC (Fig. 8d). This is close to the value reported by Jeon *et al.* (198.6 eV).[65] After 25 cycles, a broad second peak appears at 199.7 eV, which is attributed to the oxidation of chloride and the formation of ClO_x^- species.[65,89,90] The same peak is observed in the cell charged to 4.3 V and rested albeit more pronounced (Fig. 8b and c). Thus, resting at high voltages promotes more oxidation than cycling, as the cell is at high states of charge for a longer time, which enhances the growth of CEI. This is contrary to a larger LF resistance from cycling. This may be due to mechanical contact loss from NMC|LNOC delamination.[8,91] To investigate the degree of delamination in the composite cathode, FIB-SEM was conducted. Fig. S29 shows a comparison of a pristine cathode to cathodes cycled 25 times in the discharged and charged states. The pristine cathode shows residual porosity and incomplete densification. In the cycled cathodes, delamination between LNOC and NMC can be observed. However, as the pristine cathode has porosity and an incomplete densification cathode, it is difficult to quantify the degree of delamination from cycling. Nevertheless, delamination increases the LF resistance from increased diffusion lengths (*i.e.*, increasing tortuosity).[77,92,93]

Conclusions

Our in-depth study of the LMOCs|LLZTO (M = Nb, Ta, Al) hetero-electrolyte interface for dual electrolyte SSBs (*via* EIS, electron microscopy, microindentation hardness, and work of compression measurements) quantifies the soft mechanical properties of the LMOCs that enable lower fabrication and operation pressure compared to state-of-the-art sulfide electrolytes, such as argyrodite. The soft nature of LMOCs also enables a conformal LMOC|LLZTO interface at room temperature and at low stack pressures, leading to a H-E resistance $<250\ \Omega\ cm^2$ for LNOC and LTOC, and $<150\ \Omega\ cm^2$ for LAOC at 1.8 MPa. This study demonstrates the more critical role of mechanical properties over the ionic conductivity in forming a low H-E resistance. Although there is a low LMOC|LLZTO H-E resistance formed by densifying the LMOCs against the LLZTO, challenges remain to incorporate this design into a full cell. By pre-densifying the LNOC and cathode, and through a combination of the soft properties of LNOC, the Li stability with LLZTO, and a seeded silver interlayer, a Li reservoir-free LNOC|LLZTO full cell maintains high capacity ($\sim 170\ mA\ h\ g^{-1}$) and Coulombic efficiency ($>99.5\%$) down to 1 MPa at 60 °C. A Li-reservoir free cell demonstrated exceptional Coulombic efficiency ($\sim 99.8\%$) for 120 cycles at 5 MPa, maintaining 70% of the initial capacity. The capacity fade is related to the oxidation of LNOC and mechanical contact loss at the NMC|LNOC interface, which manifests as a short Warburg at low frequencies in the Nyquist plots. This degradation could be mitigated by optimizing the LNOC and conductive additive ratios in the cathode composite to improve effective ionic and electronic transport, thereby reducing tortuosity and polarization during cycling. Nevertheless, the LNOC|LLZTO H-E remains stable during cycling, further emphasizing the LNOC|LLZTO stability. Further studies are needed to address the incorporation of the low H-E resistance into a full cell at room temperature, but this study demonstrates the potential for Li reservoir-free SSBs at low pressures through an LNOC|LLZTO dual electrolyte system.

Author contributions

Max Palmer: conceptualization, investigation, methodology, data curation, and writing – original draft, review, and editing; Vipin K. Singh: conceptualization, investigation, methodology, data curation, and writing – original draft, review, and editing; Leonardo Merola: XPS formal analysis and writing – review and editing; Karthikeyen Natarajan Pugazhendhi: assisted with the bilayer symmetric cell fabrication; Pallab Barai: mesoscale modelling investigation and validation; Insang You: synthesis of LAOC SE; Yubo Wang: assisted with the synthesis of LNOC and LTOC; Eric Carlson: full cell validation; Hao Zheng: full cell validation; Cathy Wang: cathode FIB-SEM; Venkat Srinivasan: review and validation; Jürgen Janek: writing – review and editing, funding acquisition, conceptualization, and supervision; Jeff Sakamoto: writing – review and editing, funding acquisition, conceptualization, and supervision; Linda F. Nazar: writing – review and editing, funding acquisition, conceptualization, and supervision.

Conflicts of interest

The authors declare no competing financial interests.

Data availability

The data supporting this article have been included in the supplementary information (SI). The supplementary information contains Nyquist plots. distribution of relaxation time figures, and Arrhenius measurements of LLZTO, LMOCs, and bilayer symmetric cells; Modulus results and microindentation maps; Nyquist plots of full cells; Lithium plating data and SEM images of Li|LLZTO|Ag half cells; optical images of LNOC from the full cell; FIB-SEM of LMOCs and composite cathodes; Tables summarizing the triplicate measurements. See DOI: https://doi.org/10.1039/d5ee07777j.

Acknowledgements

The authors would like to acknowledge Travis Casagrande (Canadian Center for Electron Microscopy) for assisting in the FIB-SEM analysis and Hiruy Haile, Ennis Solorzano (University of Waterloo) for designing the electrochemical cell setup with force sensors. We thank Seneca Stevens (UCSB) for discussion on mechanical properties of solid electrolytes, Shu-wen Zhou (UW) for help with the full-cell fabrication, Dr Baltej Singh for the many useful discussions. This work was conducted as part of the US-German project collaboration on ''Interfaces and Interphases in Rechargeable Li-metal based Batteries'' supported by the US Department of Energy (DOE) and the German Federal Ministry of Education and Research (BMBF). L. F. N, V. K. S, and K. P are grateful to the Ontario Research Fund (ORF-RE, grant number RE-010-068) for the major financial support and the NSERC for the platform support through the Discovery Grant and the Canada Research Chair program. M. P. and J. S. acknowledge the financial support from the Mechanochemical Understanding of Solid Ion Conductors, an Energy Frontier Research Center funded by the U.S. Department of Energy, Office of Science, Office of Basic Energy Science, under the grant no. DE-SC0023438. L. M. and J. J. acknowledge the financial support from the German Federal Ministry of Education and Research (BMBF) under the project ''CatSE 2'' (grant identifier 03XP0510E). P. B. and V. S. acknowledge the support provided by the Assistant Secretary for Critical Minerals and Energy Innovation (CMEI), the Office of Transportation Technologies of the U.S. Department of Energy under Contract No. DE-AC02-06CH11357 through the Advanced Battery Materials Research (BMR) program.

References

1 P. Albertus, S. Babinec, S. Litzelman and A. Newman, *Nat. Energy*, 2017, **3**, 16–21.
2 M. J. Wang, E. Carmona, A. Gupta, P. Albertus and J. Sakamoto, *Nat. Commun.*, 2020, **11**, 5201.
3 S. E. Sandoval, C. G. Haslam, B. S. Vishnugopi, D. W. Liao, J. S. Yoon, S. H. Park, Y. Wang, D. Mitlin, K. B. Hatzell, D. J. Siegel, P. P. Mukherjee, N. P. Dasgupta, J. Sakamoto and M. T. McDowell, *Nat. Mater.*, 2025, **24**, 673–681.
4 K. B. Hatzell, *ACS Energy Lett.*, 2023, **8**, 4775–4776.
5 K. Lee, E. Kazyak, M. J. Wang, N. P. Dasgupta and J. Sakamoto, *Joule*, 2022, **6**, 2547–2565.
6 X. Zhang, Q. J. Wang, K. L. Harrison, K. Jungjohann, B. L. Boyce, S. A. Roberts, P. M. Attia and S. J. Harris, *J. Electrochem. Soc.*, 2019, **166**, A3639–A3652.
7 Y. Ren, T. Danner, A. Moy, M. Finsterbusch, T. Hamann, J. Dippell, T. Fuchs, M. Müller, R. Hoft, A. Weber, L. A. Curtiss, P. Zapol, M. Klenk, A. Ngo, P. Barai, B. Wood, R. Shi, L. Wan, T. W. Heo, M. Engels, J. Nanda, F. H. Richter, A. Latz, V. Srinivasan, J. Janek, J. Sakamoto, E. D. Wachsman and D. Fattakhova-Rohlfing, *Adv. Energy Mater.*, 2023, **13**, 2201939.
8 R. Koerver, I. Aygün, T. Leichtweiß, C. Dietrich, W. Zhang, J. O. Binder, P. Hartmann, W. G. Zeier and J. Janek, *Chem. Mater.*, 2017, **29**, 5574–5582.
9 T.-T. Zuo, R. Rueß, R. Pan, F. Walther, M. Rohnke, S. Hori, R. Kanno, D. Schröder and J. Janek, *Nat. Commun.*, 2021, **12**, 6669.
10 J. Janek and W. G. Zeier, *Nat. Energy*, 2023, **8**, 230–240.
11 K. Kerman, A. Luntz, V. Viswanathan, Y.-M. Chiang and Z. Chen, *J. Electrochem. Soc.*, 2017, **164**, A1731–A1744.
12 A. Sharafi, E. Kazyak, A. L. Davis, S. Yu, T. Thompson, D. J. Siegel, N. P. Dasgupta and J. Sakamoto, *Chem. Mater.*, 2017, **29**, 7961–7968.
13 J. G. Connell, T. Fuchs, H. Hartmann, T. Krauskopf, Y. Zhu, J. Sann, R. Garcia-Mendez, J. Sakamoto, S. Tepavcevic and J. Janek, *Chem. Mater.*, 2020, **32**, 10207–10215.
14 C. Ma, Y. Cheng, K. Yin, J. Luo, A. Sharafi, J. Sakamoto, J. Li, K. L. More, N. J. Dudney and M. Chi, *Nano Lett.*, 2016, **16**, 7030–7036.
15 Y. Kim, H. Jo, J. L. Allen, H. Choe, J. Wolfenstine and J. Sakamoto, *J. Am. Ceram. Soc.*, 2016, **99**, 1367–1374.
16 S. Yu, R. D. Schmidt, R. Garcia-Mendez, E. Herbert, N. J. Dudney, J. B. Wolfenstine, J. Sakamoto and D. J. Siegel, *Chem. Mater.*, 2016, **28**, 197–206.
17 G. Yan, J. F. Nonemacher, H. Zheng, M. Finsterbusch, J. Malzbender and M. Krüger, *J. Mater. Sci.*, 2019, **54**, 5671–5681.
18 G. Han, B. Kinzer, R. Garcia-Mendez, H. Choe, J. Wolfenstine and J. Sakamoto, *J. Eur. Ceram. Soc.*, 2020, **40**, 1999–2006.
19 M. J. Wang, R. Choudhury and J. Sakamoto, *Joule*, 2019, **3**, 2165–2178.
20 W. Zaman, L. Zhao, T. Martin, X. Zhang, Z. Wang, Q. J. Wang, S. Harris and K. B. Hatzell, *ACS Appl. Mater. Interfaces*, 2023, **15**, 37401–37409.
21 J. E. Ni, E. D. Case, J. S. Sakamoto, E. Rangasamy and J. B. Wolfenstine, *J. Mater. Sci.*, 2012, **47**, 7978–7985.
22 T. Demuth, T. Fuchs, F. Walther, A. Pokle, S. Ahmed, M. Malaki, A. Beyer, J. Janek and K. Volz, *Matter*, 2023, **6**, 2324–2339.

23 L. Miara, A. Windmüller, C.-L. Tsai, W. D. Richards, Q. Ma, S. Uhlenbruck, O. Guillon and G. Ceder, *ACS Appl. Mater. Interfaces*, 2016, **8**, 26842–26850.
24 L. M. Riegger, R. Schlem, J. Sann, W. G. Zeier and J. Janek, *Angew. Chem.*, 2021, **133**, 6792–6797.
25 L. M. Riegger, S.-K. Otto, M. Sadowski, S. Jovanovic, O. Kötz, S. Harm, L. G. Balzat, S. Merz, S. Burkhardt, F. H. Richter, J. Sann, R.-A. Eichel, B. V. Lotsch, J. Granwehr, K. Albe and J. Janek, *Chem. Mater.*, 2022, **34**, 3659–3669.
26 S. Wenzel, S. J. Sedlmaier, C. Dietrich, W. G. Zeier and J. Janek, *Solid State Ionics*, 2018, **318**, 102–112.
27 G. F. Dewald, S. Ohno, M. A. Kraft, R. Koerver, P. Till, N. M. Vargas-Barbosa, J. Janek and W. G. Zeier, *Chem. Mater.*, 2019, **31**, 8328–8337.
28 L. Zhou, T.-T. Zuo, C. Y. Kwok, S. Y. Kim, A. Assoud, Q. Zhang, J. Janek and L. F. Nazar, *Nat. Energy*, 2022, **7**, 83–93.
29 Y. Tanaka, K. Ueno, K. Mizuno, K. Takeuchi, T. Asano and A. Sakai, *Angew. Chem., Int. Ed.*, 2023, **62**, e202217581.
30 K.-H. Park, K. Kaup, A. Assoud, Q. Zhang, X. Wu and L. F. Nazar, *ACS Energy Lett.*, 2020, **5**, 533–539.
31 I. Kochetkov, T.-T. Zuo, R. Ruess, B. Singh, L. Zhou, K. Kaup, J. Janek and L. Nazar, *Energy Environ. Sci.*, 2022, **15**, 3933–3944.
32 B. Hennequart, M. Platonova, R. Chometon, T. Marchandier, A. Benedetto, E. Quemin, R. Dugas, C. Lethien and J.-M. Tarascon, *ACS Energy Lett.*, 2024, **9**, 454–460.
33 J. Hüttl, C. Seidl, H. Auer, K. Nikolowski, A. L. Görne, M. Arnold, C. Heubner, M. Wolter and A. Michaelis, *Energy Storage Mater.*, 2021, **40**, 259–267.
34 M. Palmer, L. Qian, V. K. Singh, L. Merola, E. Carlson, C. Haslam, J. Janek, L. F. Nazar and J. Sakamoto, *Solid State Ionics*, 2025, **428**, 116948.
35 L. Merola, V. K. Singh, M. Palmer, J. K. Eckhardt, S. L. Benz, T. Fuchs, L. F. Nazar, J. Sakamoto, F. H. Richter and J. Janek, *ACS Appl. Mater. Interfaces*, 2024, **16**(40), 54847–54863.
36 T. Lee, S. Joo, S. Kang, T. Kim, Y. Park, Y. Chae, K. Kim, W. Cho and S. Kim, *ACS Appl. Energy Mater.*, 2025, **8**, 5585–5611.
37 J. K. Eckhardt, S. Kremer, L. Merola and J. Janek, *ACS Appl. Mater. Interfaces*, 2024, **16**, 18222–18235.
38 J. Fleig and J. Maier, *J. Electrochem. Soc.*, 1997, **144**, L302–L305.
39 M. Klimpel, C. Černe, J. Šivavec, J. F. Baumgärtner, H. Zhang, R. Widmer, F. Okur, F. Krumeich, K. V. Kravchyk and M. V. Kovalenko, *ACS Appl. Energy Mater.*, 2025, **8**(21), 15900–15910.
40 D. P. Abraham, D. W. Dees, J. Knuth, E. Reynolds, R. Gerald, Y.-E. Hyung, I. Belharouak, M. Stoll, E. Sammann, S. MacLaren, R. Haasch, R. Twesten, M. Sardela, V. Battaglia, E. Cairns, J. Kerr, M. Kerlau, R. Kostecki, J. Lei, K. McCarthy, F. McLarnon, J. Reimer, T. Richardson, P. Ross, S. Sloop, X. Song, V. Zhuang, M. Balasubramanian, J. McBreen, K.-Y. Chung, X. Q. Yang, W.-S. Yoon and L. Norin, *Diagnostic examination of Generation 2 lithium-ion cells and assessment of performance degradation mechanisms*, 2005.
41 Y. Leng, S. Ge, D. Marple, X.-G. Yang, C. Bauer, P. Lamp and C.-Y. Wang, *J. Electrochem. Soc.*, 2017, **164**, A1037–A1049.
42 J. B. Quinn, T. Waldmann, K. Richter, M. Kasper and M. Wohlfahrt-Mehrens, *J. Electrochem. Soc.*, 2018, **165**, A3284–A3291.
43 I. You, B. Singh, M. Cui, G. Goward, L. Qian, Z. Arthur, G. King and L. F. Nazar, *Energy Environ. Sci.*, 2025, **18**, 478–491.
44 B. Singh, Y. Wang, J. Liu, J. D. Bazak, A. Shyamsunder and L. F. Nazar, *J. Am. Chem. Soc.*, 2024, **146**, 17158–17169.
45 T. Dai, S. Wu, Y. Lu, Y. Yang, Y. Liu, C. Chang, X. Rong, R. Xiao, J. Zhao, Y. Liu, W. Wang, L. Chen and Y.-S. Hu, *Nat. Energy*, 2023, **8**, 1221–1228.
46 W. Kim, S. Han, S. Lee, J. Yoo, C. Park, S. Yu, D. Won, E. Lee, K. Ko, J. Noh, G. Choi, M. Kim and K. Kang, *Energy Environ. Sci.*, 2025, **18**, 8039–8051.
47 J.-M. Doux, Y. Yang, D. H. S. Tan, H. Nguyen, E. A. Wu, X. Wang, A. Banerjee and Y. S. Meng, *J. Mater. Chem. A*, 2020, **8**, 5049–5055.
48 Y. Wang, H. Hao, K. G. Naik, B. S. Vishnugopi, C. D. Fincher, Q. Yan, V. Raj, H. Celio, G. Yang, H. Fang, Y. Chiang, F. A. Perras, P. Jena, J. Watt, P. P. Mukherjee and D. Mitlin, *Adv. Energy Mater.*, 2024, **14**, 2304530.
49 C. Rosenbach, F. Walther, J. Ruhl, M. Hartmann, T. A. Hendriks, S. Ohno, J. Janek and W. G. Zeier, *Adv. Energy Mater.*, 2023, **13**, 2203673.
50 S. Pacetti, C. Karlsson, E. Mijit, M. Drüschler, A. Di Cicco, N. Pinto, D. Bresser and J. Rezvani, *J. Phys. Chem. C*, 2026, **130**, 3040–3049.
51 I. Rashid, R. R. Haddadin, A. A. Alkafaween, R. N. Alkaraki and R. M. Alkasasbeh, *AAPS Open*, 2022, **8**, 6.
52 M. Papakyriakou, M. Lu, Y. Liu, Z. Liu, H. Chen, M. T. McDowell and S. Xia, *J. Power Sources*, 2021, **516**, 230672.
53 S.-Y. Lee, J.-H. Han, H.-W. Gong, J. Ahn, K.-W. Yi and Y. W. Cho, *J. Mater. Chem. A*, 2025, **13**, 6342–6346.
54 K. Hikima, M. Totani, S. Obokata, H. Muto and A. Matsuda, *ACS Appl. Energy Mater.*, 2022, **5**, 2349–2355.
55 P. Barai, T. Kinnibrugh, M. Wolfman, J. Garcia, X. Wang, T. T. Fister, H. Iddir and V. Srinivasan, *JOM*, 2024, **76**, 1180–1191.
56 T. Zuo, F. Walther, J. H. Teo, R. Rueß, Y. Wang, M. Rohnke, D. Schröder, L. F. Nazar and J. Janek, *Angew. Chem., Int. Ed.*, 2023, **62**, e202213228.
57 Y. U. Wang, *Acta Mater.*, 2006, **54**, 953–961.
58 F. Raether, G. Seifert and H. Ziebold, *Adv. Theory Sims.*, 2019, **2**, 1900048.
59 A. Gupta and J. Sakamoto, *Electrochem. Soc. Interface*, 2019, **28**, 63.
60 T. Krauskopf, H. Hartmann, W. G. Zeier and J. Janek, *ACS Appl. Mater. Interfaces*, 2019, **11**, 14463–14477.
61 L. Pastewka and M. O. Robbins, *Proc. Natl. Acad. Sci. U. S. A.*, 2014, **111**, 3298–3303.
62 B. N. J. Persson, *Surf. Sci. Rep.*, 2006, **61**, 201–227.
63 H. Huo, J. Luo, V. Thangadurai, X. Guo, C.-W. Nan and X. Sun, *ACS Energy Lett.*, 2020, **5**, 252–262.

64 S. Wang, E. Barks, P.-T. Lin, X. Xu, C. Melamed, G. McConohy, S. Nemšák and W. C. Chueh, *Chem. Mater.*, 2024, **36**, 6849–6864.
65 S. Jeon, K.-H. Park, W. Cho, G. Jeong, J. Yu, Y. J. Park and K. Kim, *Solid State Ionics*, 2025, **421**, 116791.
66 J. A. Newnham, J. Kondek, J. Hartel, C. Rosenbach, C. Li, V. Faka, L. Gronych, D. Glikman, F. Schreiner, D. D. Wind, B. Braunschweig, M. R. Hansen and W. G. Zeier, *Chem. Mater.*, 2025, **37**, 4130–4144.
67 S. Adams, *Energy Storage Mater.*, 2024, **68**, 103359.
68 M. Siniscalchi, J. S. Gibson, J. Tufnail, J. E. N. Swallow, J. Lewis, G. Matthews, B. Karagoz, M. A. Van Spronsen, G. Held, R. S. Weatherup, C. R. M. Grovenor and S. C. Speller, *ACS Appl. Mater. Interfaces*, 2024, **16**, 27230–27241.
69 A. Shyamsunder, M. Palmer, I. R. Kochetkov, J. S. Sakamoto and L. F. Nazar, *ACS Appl. Mater. Interfaces*, 2023, **15**(45), 52571–52580.
70 H. Huo, Y. Chen, N. Zhao, X. Lin, J. Luo, X. Yang, Y. Liu, X. Guo and X. Sun, *Nano Energy*, 2019, **61**, 119–125.
71 Y. Ruan, Y. Lu, X. Huang, J. Su, C. Sun, J. Jin and Z. Wen, *J. Mater. Chem. A*, 2019, **7**, 14565–14574.
72 S. Koch, *Solid State Ionics*, 2004, **168**, 1–11.
73 P. Minnmann, J. Schubert, S. Kremer, R. Rekers, S. Burkhardt, R. Ruess, A. Bielefeld, F. H. Richter and J. Janek, *J. Electrochem. Soc.*, 2024, **171**, 060514.
74 H. Kim, S. Park, S. Kang, J. Y. Jung, K. Kim, J. Yu, D. Kim, J. Lee, Y. Sun and W. Cho, *Adv. Funct. Mater.*, 2024, **34**, 2409318.
75 F. Walther, S. Randau, Y. Schneider, J. Sann, M. Rohnke, F. H. Richter, W. G. Zeier and J. Janek, *Chem. Mater.*, 2020, **32**, 6123–6136.
76 M. Kissel, M. Schosland, J. Töws, D. Kalita, Y. Schneider, J. Kessler-Kühn, S. Schröder, J. Schubert, F. Frankenberg, A. Kwade, A. Bielefeld, F. H. Richter and J. Janek, *Adv. Energy Mater.*, 2025, **15**, 2405405.
77 H.-C. Yu, S. B. Adler, S. A. Barnett and K. Thornton, *Electrochim. Acta*, 2020, **354**, 136534.
78 C. Haslam and J. Sakamoto, *J. Electrochem. Soc.*, 2023, **170**, 040524.
79 D.-S. Ko, S. Kim, S. Lee, G. Yoon, D. Kim, C. Shin, D. Kim, J. Lee, S. Sul, D.-J. Yun and C. Jung, *Nat. Commun.*, 2025, **16**, 1066.
80 S. E. Sandoval, J. A. Lewis, B. S. Vishnugopi, D. L. Nelson, M. M. Schneider, F. J. Q. Cortes, C. M. Matthews, J. Watt, M. Tian, P. Shevchenko, P. P. Mukherjee and M. T. McDowell, *Joule*, 2023, **7**, 2054–2073.
81 S. H. Choi, C. H. Baek, J. Oh, G.-J. Lee, M. Kim, H. Lee, D.-J. Yoo, Y. S. Jung, K. Kim, J.-S. Yu, W. Cho, H. Park and J. W. Choi, *Nat. Commun.*, 2025, **16**, 5871.
82 J. Thomas, S. S. Behara and A. Van Der Ven, *Chem. Mater.*, 2024, 4c01903.
83 A. D. Pelton, *Bull. Alloy Phase Diagrams*, 1986, **7**, 223–228.
84 S. Jin, Y. Ye, Y. Niu, Y. Xu, H. Jin, J. Wang, Z. Sun, A. Cao, X. Wu, Y. Luo, H. Ji and L.-J. Wan, *J. Am. Chem. Soc.*, 2020, **142**, 8818–8826.
85 K. Yan, Z. Lu, H.-W. Lee, F. Xiong, P.-C. Hsu, Y. Li, J. Zhao, S. Chu and Y. Cui, *Nat. Energy*, 2016, **1**, 16010.
86 Y.-G. Lee, S. Fujiki, C. Jung, N. Suzuki, N. Yashiro, R. Omoda, D.-S. Ko, T. Shiratsuchi, T. Sugimoto, S. Ryu, J. H. Ku, T. Watanabe, Y. Park, Y. Aihara, D. Im and I. T. Han, *Nat. Energy*, 2020, **5**, 299–308.
87 M. S. R. Limon, C. W. Duffee and Z. Ahmad, *ACS Energy Lett.*, 2025, **10**, 1999–2006.
88 W. Kim, J. Noh, S. Lee, K. Yoon, S. Han, S. Yu, K. Ko and K. Kang, *Adv. Mater.*, 2023, **35**, 2301631.
89 Z. Song, T. Wang, H. Yang, W. H. Kan, Y. Chen, Q. Yu, L. Wang, Y. Zhang, Y. Dai, H. Chen, W. Yin, T. Honda, M. Avdeev, H. Xu, J. Ma, Y. Huang and W. Luo, *Nat. Commun.*, 2024, **15**, 1481.
90 L. Zhou, J. D. Bazak, C. Li and L. F. Nazar, *ACS Energy Lett.*, 2024, **9**, 4093–4101.
91 T. Shi, Y.-Q. Zhang, Q. Tu, Y. Wang, M. C. Scott and G. Ceder, *J. Mater. Chem. A*, 2020, **8**, 17399–17404.
92 C. König, V. Miß, L. Janin and B. Roling, *ACS Appl. Energy Mater.*, 2023, **6**, 9356–9362.
93 A. C. Lazanas and M. I. Prodromidis, *ACS Meas. Sci. Au*, 2023, **3**, 162–193.